

---

## Reaction Dynamics and Charge Transfer in the Scattering of State-Selected Ions on Surfaces

Patricia L. Maazouz

### Publication Date

15-04-2004

### License

This work is made available under a All Rights Reserved license and should only be used in accordance with that license.

### Citation for this work (American Psychological Association 7th edition)

Maazouz, P. L. (2004). *Reaction Dynamics and Charge Transfer in the Scattering of State-Selected Ions on Surfaces* (Version 1). University of Notre Dame. <https://doi.org/10.7274/7h149p30z5r>

This work was downloaded from CurateND, the University of Notre Dame's institutional repository.

For more information about this work, to report or an issue, or to preserve and share your original work, please contact the CurateND team for assistance at [curate@nd.edu](mailto:curate@nd.edu).

## CHAPTER 4

### DISSOCIATION DYNAMICS: $\text{Br}_2^+$ + Pt(111)

#### 4.1. Introduction

Experimental results from atomic bromine scattering on Pt(111) revealed an unusual scattering behavior which results in efficient charge and energy transfer near the resonance. It was suggested that the resonance arises from the electronic coupling between the departing projectile and the surface deformation created at impact. The study represents the first experimental evidence for such coupling. In order to learn more about this behavior and investigate its generality, the investigation is extended to molecular bromine projectiles. Specifically, the dynamics of dissociation and negative ion formation are investigated in the scattering of state-selected  $\text{Br}_2^+$  on Pt(111).

In addition to measuring the probability for negative ion formation and the corresponding exit angles and kinetic energies, the experimental apparatus described in Chapter 2 is uniquely designed to investigate the reaction dynamic's sensitivity to the incident projectile's vibrational energy. An examination of the potential energy curves for the bromine molecule reveals that the amount of vibrational energy in the incident projectile may play an important role in the reaction dynamics. Figure 4.1 shows the  $\text{Br}_2^+$ ,  $\text{Br}_2$ , and  $\text{Br}_2^-$  potential energy curves that are most likely to participate in electron transfer processes when the bromine projectiles are in close proximity to

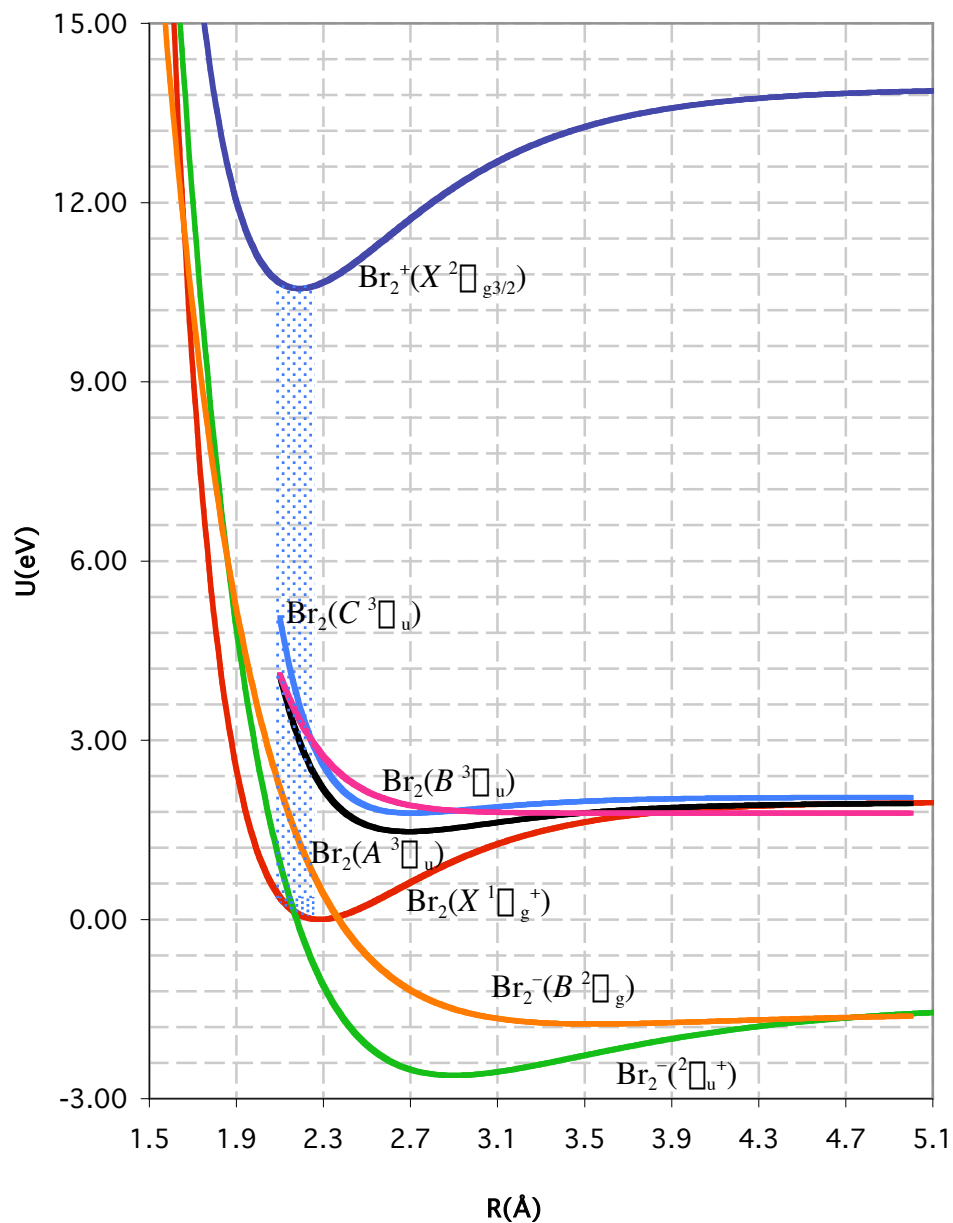
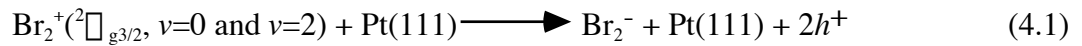


Figure 4.1. Potential energy curves for bromine that may participate in the scattering of state-selected  $\text{Br}_2^+$  on Pt(111). The parameters for the curves are obtained from various sources  $\text{Br}_2^+(X^2g_{3/2})$ ,  $\text{Br}_2(X^1g^+)$ ,  $\text{Br}_2(A^3u)$ ,  $\text{Br}_2(B^3u)$ ,  $\text{Br}_2(C^1u)$ ,  $\text{Br}_2^-(^2u^+)$ ,  $\text{Br}_2^-(B^2g_{3/2})$ .<sup>1,2,3,4,5</sup>

the Pt(111) surface. The shaded region in Fig. 4.1 reveals that  $\text{Br}_2^+$  molecules prepared in the ground vibrational state can neutralize to the ground electronic  $\text{Br}_2(X^1\Sigma_g^+)$ , or to the repulsive part of the  $A$ ,  $B$ , or  $C$  excited states. A change in the incident vibrational energy will modify the Franck-Condon overlap between the state-selected molecular cations and the neutral bromine molecules. Therefore, the probability for the incident projectile to neutralize into a particular electronic state is expected to depend on the amount of initial vibrational energy. After the incident molecule neutralizes, a second electron can transfer from the surface to the projectile forming  $\text{Br}_2^-$  in the ground or an excited electronic state. The details for these electron transfer processes are investigated for scattering state-selected  $\text{Br}_2^+$  molecules on a well-characterized Pt(111) surface.

This chapter investigates the reaction dynamics when state-selected bromine molecular cations scatter from Pt(111). Equations 4.1 and 4.2 describe the chemical reactions for the negative ion formation and dissociation processes observed in this system,



where  $h^+$  represents an electron hole formed at the Pt surface. The probability to form  $\text{Br}_2^-$  and  $\text{Br}^-$  products is measured as a function of the incident  $\text{Br}_2^+$  translational and vibrational energy and of the surface temperature. Finally, the critical experimental factors for obtaining the resonance feature are discussed when the results for scattering  $\text{Br}_2^+$  are compared to the results for scattering state-selected  $\text{Br}^+$  on Pt(111).

## 4.2. Experiment

State-selected  $\text{Br}_2^+$  ions are prepared via 2+1 resonance enhanced multiphoton ionization (REMPI) via the excitation of ground state  $\text{Br}_2$  through the intermediate state with a specified core electronic configuration. Prior to an experiment, the desired REMPI transition is determined by using the time-of-flight detector to monitor the ion signal as a function of the laser wavelength. The REMPI spectroscopy for molecular bromine in the 68000 to 73400  $\text{cm}^{-1}$  region is well documented.<sup>6</sup> A particular transition can be selected to form  $\text{Br}_2^+$  ions in a specific electronic and vibrational state as summarized in Table 4.1.

TABLE 4.1. STATE-SELECTED  $\text{Br}_2^+$  ROVIBRATIONAL PURITY

Two-Photon Energy( $\text{cm}^{-1}$ )	Dye Laser $\lambda$ (nm)	Ion Core	Final $v^+$ Level	Purity
68825	581.15	$2\sigma_{g3/2}$	0	95
69190	578.12	$2\sigma_{g3/2}$	1	95
70568	566.83	$2\sigma_{g3/2}$	0	79
70939	563.86	$2\sigma_{g3/2}$	1	79
71336	560.73	$2\sigma_{g3/2}$	2	79
71750	557.49	$2\sigma_{g1/2}$	0	94
72157	554.35	$2\sigma_{g1/2}$	1	94
72440	552.18	$2\sigma_{g3/2}$	0	100
72904	548.67	$2\sigma_{g3/2}$	0	90
73271	545.92	$2\sigma_{g3/2}$	1	90

Note: Purity of state-selected  $\text{Br}_2^+$  molecules as determined by Koenders *et. al.*<sup>6</sup> Two photons from the frequency-doubled output of the dye laser are used to excite each transition.

In the current experiments, the dye laser wavelength is 552.149 nm to exclusively create bromine molecules in the ground electronic state,  $^2\Pi_{g3/2}$ , with zero quanta of vibrational energy. To investigate the effects of vibrational energy on the reaction dynamics, the dye laser wavelength is shifted to 560.617 nm, corresponding to the formation of  $\text{Br}_2^+(^2\Pi_{g3/2}, v=2)$  molecules. The REMPI transition is highly sensitive to bromine isotope effects, which requires careful selection of the laser wavelength to ensure that the proportion of the  $^{79}\text{Br}_2$ ,  $^{79}\text{Br}^{81}\text{Br}$ , and  $^{81}\text{Br}_2$  TOF signals is consistent with the natural abundance (50.54%  $^{79}\text{Br}$ , 49.46%  $^{81}\text{Br}$ ) for these isotopes. The dye laser wavelength is held constant throughout the experiments for a particular vibrational state. However, when switching between the wavelengths the Autotracking tilt angle for the doubling crystal unit is adjusted to produce a similar number of incident projectiles for the two vibrational states. When the number of state-selected ions saturates the detector, the laser intensity is reduced by minor adjustments to the tilt angle of the doubling crystal in the Autotracker unit.

The state-selected ions are extracted, accelerated, mass-selected, and finally decelerated to the final translational energy between 24 and 84 eV before impinging normal to a clean, well-characterized Pt(111) single crystal surface as described in Section 3.2. The swat delays for the incident bromine molecules ranged between 46.1  $\mu\text{s}$  and 30.2  $\mu\text{s}$  for 7 eV and 100 eV ion packets, respectively. A time-of-flight mass scan revealed that the mass delay, the flight time between the repeller plates and the CEMA plates, for incident  $\text{Br}_2^+$  is 2315 ns. The final collision energy calibration for each ion packet is performed by measuring the number of deflected incident ions as a function of the voltage potential on the deflector plate. For the bromine ion packets, the calibrated energies are shifted by 3.5 to 4 eV to higher energies compared to the ion optics final energy input values.

The scattered product yields are monitored with the two-dimensional ion-imaging detector described in Sect. 2.5.1. For each incident energy a series of ten swat delays

with 1 –2 ps increments are chosen to give optimum results for the velocity distribution (Sect. 2.6). Scattered product images, collected at several different repeller pulse delays are processed together into a single polar velocity map. Each map represents the probability density for each product as a function of final scattering angle and velocity.

### 4.3. Results and Discussion

#### 4.3.1. Scattering $\text{Br}_2^+(\nu = 0)$ on Pt(111) at 25°C

The detailed reaction dynamics are investigated for state-selected bromine molecules colliding normal to a Pt(111) surface at  $T_s = 25^\circ \text{C}$ . In order to compare the dynamics for scattering atomic and molecular projectiles, the results described in this section utilized incident projectiles with only zero quanta of vibrational energy, unless otherwise noted. For  $\text{Br}_2^+(\nu_{g3/2}, \nu=0)$  projectiles with translational energies between 24 and 84 eV, only  $\text{Br}_2^-$  and  $\text{Br}^-$  ionic products with peak mass delays near 2300 ps and 1600 ps, respectively, are detected within the limits of the detector. The absolute yields, scattered velocities, and angular distributions for both scattered species are measured when the surface is held at room temperature.

The intensities of the scattered  $\text{Br}^-$  and  $\text{Br}_2^-$  products are measured as a function of the exit velocity and final scattering angles for several  $\text{Br}_2^+(\nu_{g3/2}, \nu=0)$  collision energies. Figure 4.2 shows representative results for 24, 43.5, and 83.5 eV  $\text{Br}_2^+$  collision energies where black and white represents the maximum and minimum intensities, respectively. The maximum  $\text{Br}^-$  and  $\text{Br}_2^-$  product yields occur for the backscattered ions at  $0^\circ$ , regardless of the  $\text{Br}_2^+$  incident velocity. As the scattering

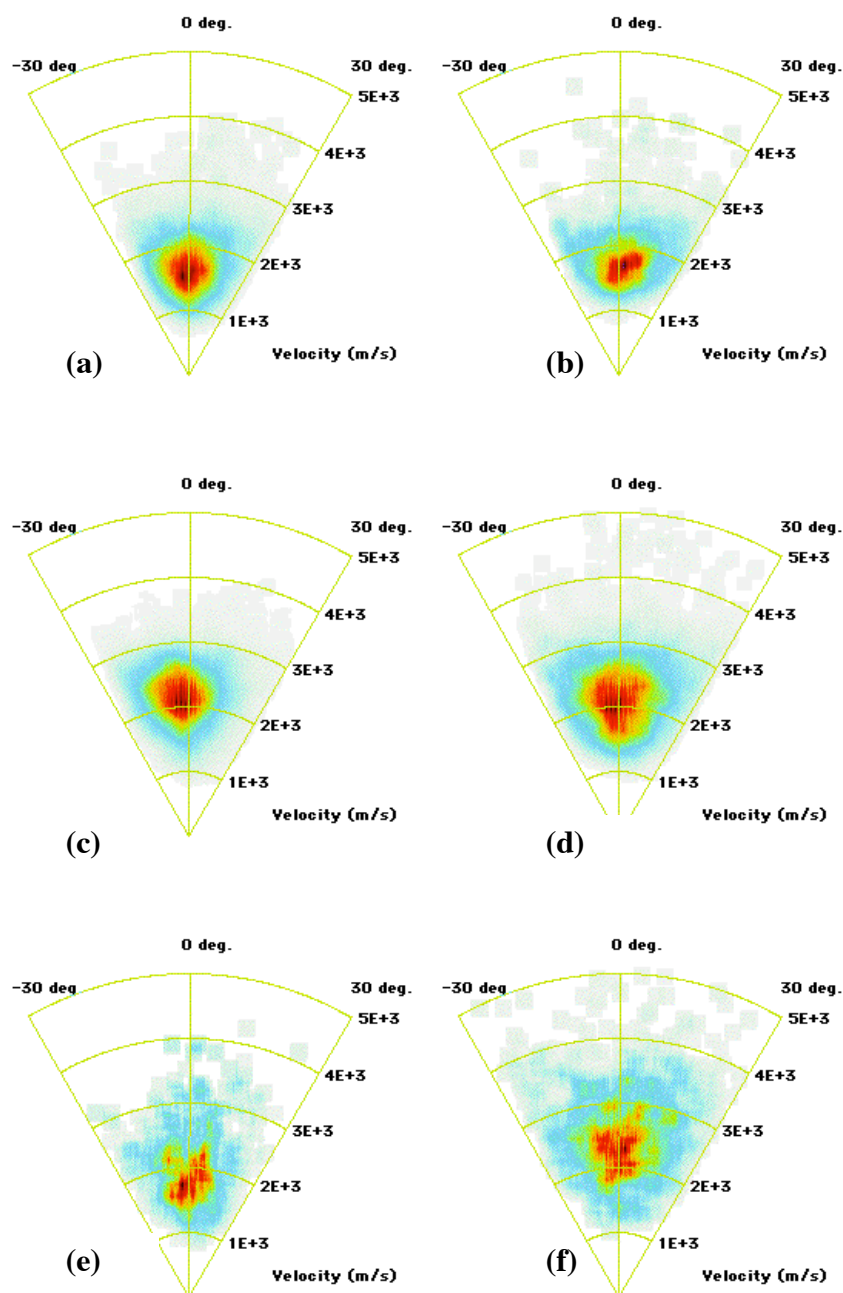


Figure 4.2. The  $\text{Br}_2^-$  (a, c, and e) and  $\text{Br}^-$  (b, d, and f) product yield intensities versus scattered velocities and angles for  $\text{Br}_2^+$  collision energies (a) and (b) 5.38 km/s (24 eV), (c) and (d) 7.25 km/s (43.5 eV), and (e) and (f) 10.04 km/s (83.5 eV). White indicates the lowest product yield and black indicates the highest intensity for negative ion formation.



angle moves off-normal, the product intensity continually decreases. Qualitatively, the  $\text{Br}^-$  products appear to leave the surface with a broader angular distribution compared to  $\text{Br}_2^-$ . However, for the same  $\text{Br}_2^+$  kinetic energy, the two products appear to leave the surface with similar exit velocities. The overall shape of the scattered product intensities is very sensitive to the  $\text{Br}^+$  translational energy, where the most focused polar maps occur for collision energies between 40 and 50 eV. In order to quantify these intriguing scattering behaviors, the data is represented in various two-dimensional plots.

When the data from Fig. 4.2 is averaged over all angles, a one-dimensional velocity distribution is obtained. Figure 4.3 shows a series of velocity distributions recorded for the  $\text{Br}_2^-$  and  $\text{Br}^-$  products. The distribution for each product is measured at a different incident  $\text{Br}_2^+(\sqrt{2}\mu_{\text{g}^{3/2}}, v=0)$  kinetic energy as indicated in the figure. The red and black dashed curves in Fig. 4.3 trace the  $\text{Br}_2^-$  and  $\text{Br}^-$  peak velocities, respectively, as a function of the incident energy. For collision velocities below 8.1 km/s, the most probable exit velocity for both products gradually increases with increasing collision velocity. More interestingly, the peak positions for the two products are very near coincident in this energy regime. However, for incident velocities greater than 8.1 km/s, the molecular and atomic products leave the surface with very different velocity distributions. In this higher incident velocity regime, the peak velocity for scattered  $\text{Br}_2^-$  *decreases* with increasing  $\text{Br}_2^+$  collision velocity, which is the opposite trend observed for scattered  $\text{Br}^-$ . This coupling and uncoupling behavior for the two products suggests that different types of reactive scattering occur within distinct incident-velocity regimes.

The relative product yields as a function of the collision velocity are obtained when each plot from Fig 4.3 is integrated with respect to the exit velocities. These relative yield values are compared to the  $\text{Br}^-(^1S_0)$  product yield results described in Chapter 3 for  $\text{Br}^+(^3P_2)$  scattered from Pt(111). Figure 4.4 clearly shows the extreme

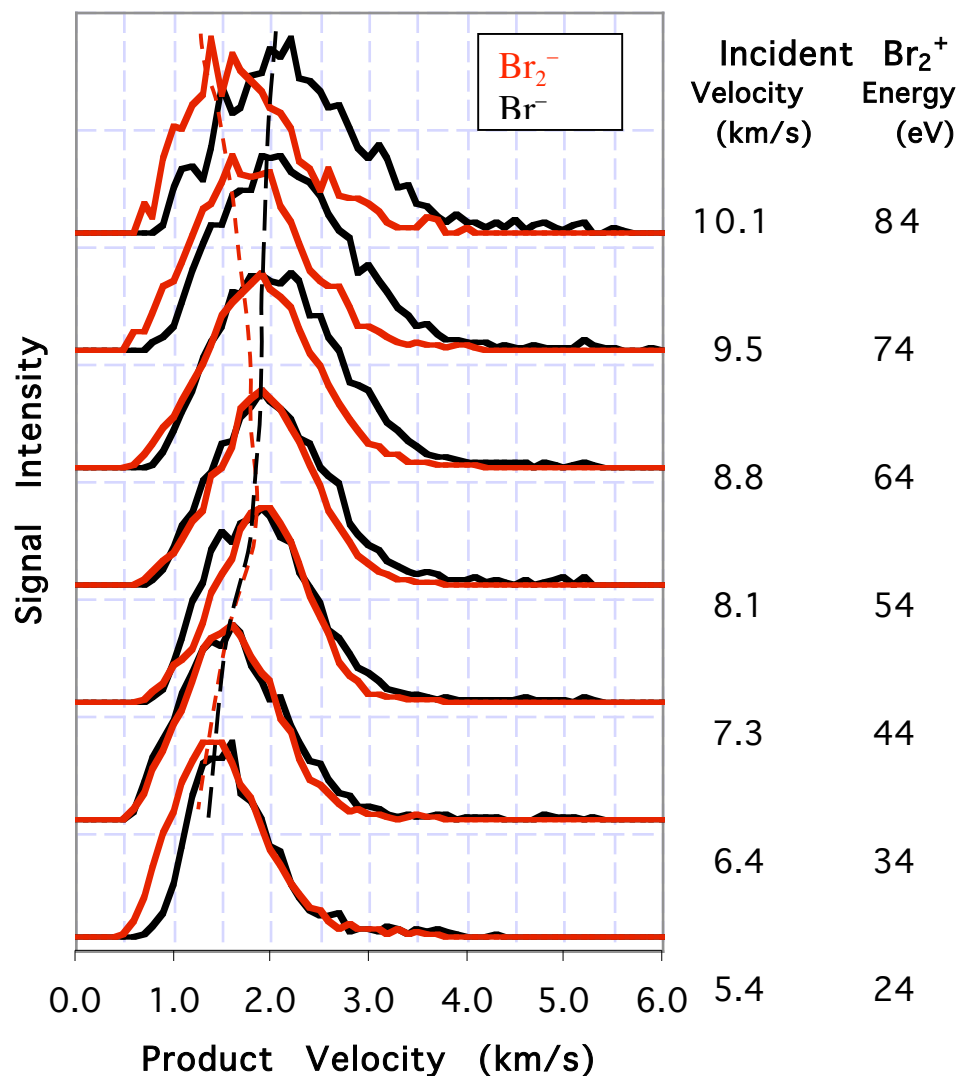


Figure 4.3. A series of product  $\text{Br}^-$  (black) and  $\text{Br}_2^-$  (red) velocity distributions for various incident  $\text{Br}_2^+(^2\Pi_{g3/2}, v=0)$  energies on Pt(111),  $T_s=25^\circ\text{C}$ . All velocity distributions are rescaled to share a common peak intensity. The incident velocity and corresponding kinetic energy for  $\text{Br}_2^+$  is indicated next to each distribution. The dashed curves track the most probable exit velocities for each product.

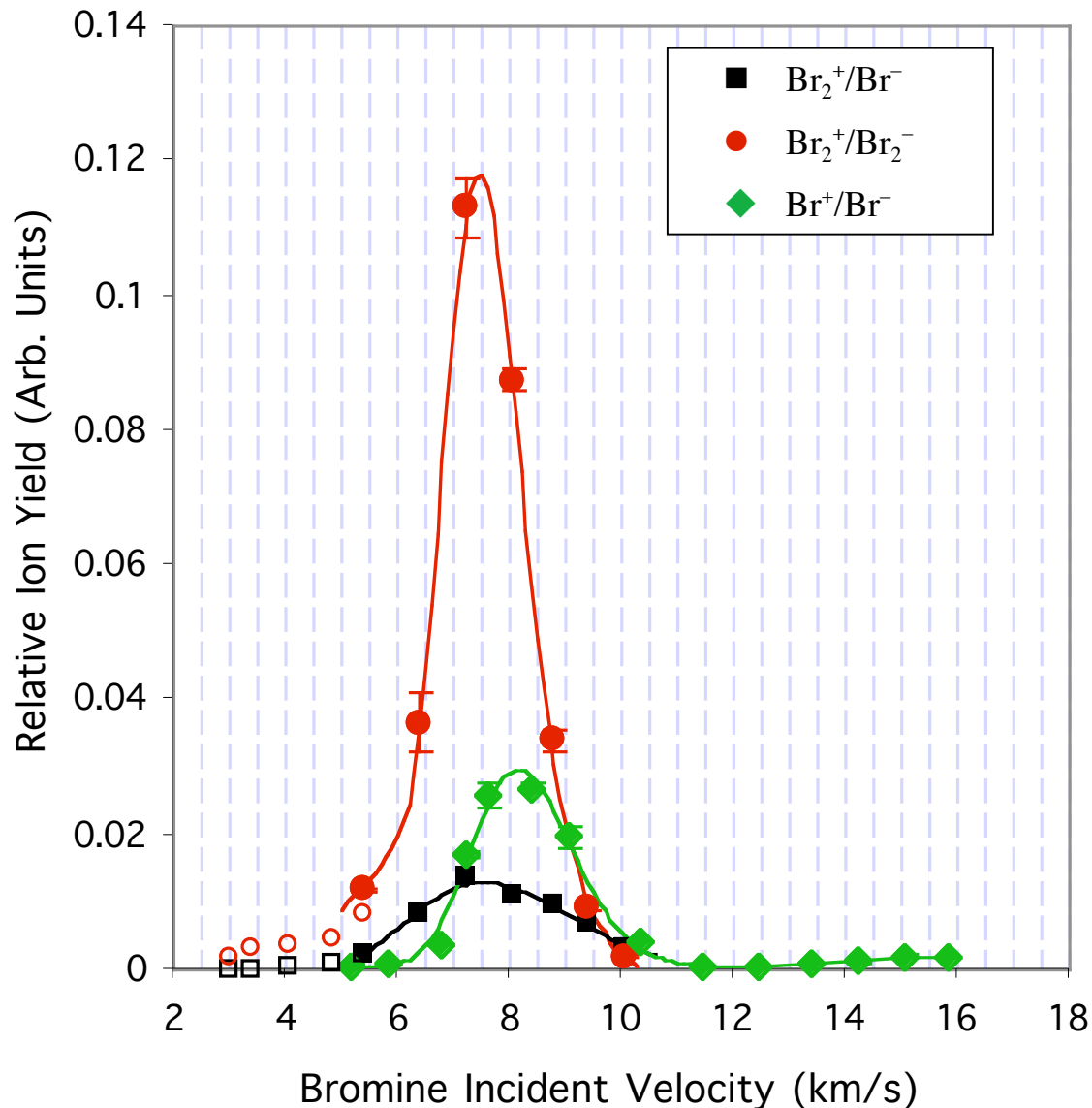


Figure 4.4. Relative yield of scattered  $\text{Br}_2^-$  and  $\text{Br}^-$  versus collision velocity for  $\text{Br}_2^+(^2\Pi_{g3/2}, v=0)$  incident on room temperature Pt(111). The relative yields for  $\text{Br}^-(^1S_0)$  resulting from scattering  $\text{Br}^+(^3P_2)$  on Pt(111) are overlaid for comparison. The open circles ( $\text{Br}_2^-$ ) and squares ( $\text{Br}^-$ ) represent data collected for  $\text{Br}_2^+$  under different experimental conditions. The curves are drawn to guide the eye.

sensitivity of the negative ion formation to the initial translational energy, especially for scattered  $\text{Br}_2^-$ . When the collision velocity increases or decreases by only 1 km/s from the peak of the resonance, the  $\text{Br}_2^-$  yield drops by almost a factor of 5. Given the solid angle of collection for the detector and the measured angular distribution of the products, it is estimated that the total anion yield is approximately 2.5 times the relative yield reported in Fig. 4.3.<sup>7</sup> Accordingly, the resonance feature near 7.5 km/s converts approximately 30% of the incident  $\text{Br}_2^+$  ions into scattered  $\text{Br}_2^-$  products. The  $\text{Br}^-$  yield resulting from incident  $\text{Br}_2^+$  also exhibits a much smaller resonance feature coincident with the peak at 7.5 km/s observed for  $\text{Br}_2^-$ . Surprisingly, the atomic bromine negative ion yield is almost an order of magnitude less than the  $\text{Br}_2^-$  yield near the resonance peak velocity.

Figure 4.5 shows the dependence of the scattered  $\text{Br}_2^-$  and  $\text{Br}^-$  exit velocities on the  $\text{Br}_2^+(\theta_{\text{g3/2}}, v=0)$  incident velocities. Again, the results for scattered bromine atomic cations are overlaid on the plot for comparison. Across the incident  $\text{Br}_2^+$  velocity range explored, the  $\text{Br}^-$  fragments leave the surface with higher velocities compared to  $\text{Br}_2^-$ . As the collision velocity increases above 7 km/s, the difference between the product velocities also increases. The mean exit velocity for scattered  $\text{Br}^-$  depends almost linearly on the incident kinetic energy compared to the  $\text{Br}_2^-$  molecules that leave the surface with a maximum velocity near 7 km/s, coincident with the resonance feature observed in Fig. 4.4. This unusual relationship between the exit velocities for the two products is very important to consider when assigning particular mechanisms for the scattering mechanisms.

The relationship between the data in Figs. 4.4 and 4.5 is also very informative. For example, a comparison of the scattering behavior for 7.3 km/s and 8.8 km/s  $\text{Br}_2^+$  indicates that in both cases, the scattered  $\text{Br}_2^-$  products leave the surface with a mean velocity of 2.1 km/s. Thus both scattering conditions should produce a similar anion

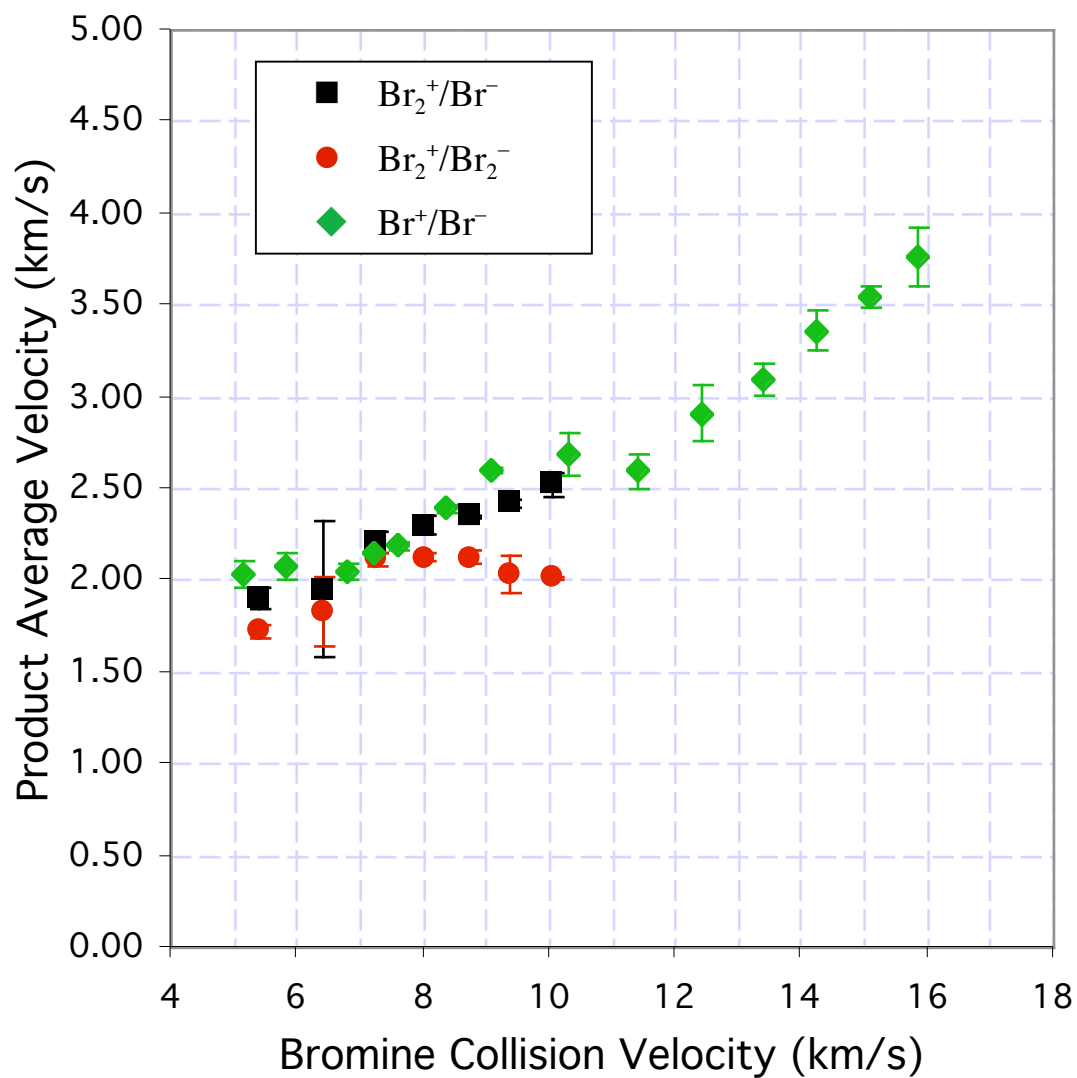


Figure 4.5. Mean exit velocities of scattered  $\text{Br}_2^-$  and  $\text{Br}^-$  products as a function of projectile velocity. The squares and circles represent the products from  $\text{Br}_2^+(^2\Pi_{g3/2}, v=0)$  projectiles, and the diamonds represent the  $\text{Br}^-(^1S_0)$  products for incident  $\text{Br}^+(^3P_2)$  projectiles. The error bars indicate 90% confidence limits in the data.

yield, if the final charge-state depends only on the outgoing velocity. Yet, the relative yield for 7.3 km/s  $\text{Br}_2^+$  is more than three times greater than the relative yield corresponding to 8.8 km/s  $\text{Br}_2^+$ . Contrary to conventional charge-transfer theories, the probability for electron transfer depends on the entire scattering trajectory, not just the exit velocities of the products, as observed for scattered  $\text{Br}^+$  on Pt(111) (See Chapter 3).

Additional insight into the mechanism responsible for the unusual scattering behavior is obtained when the data from Fig. 4.2 is integrated over all exit velocities. The resulting polar intensity plots illustrate the absolute product yield as a function of the exit angle. Representative plots for 5.38 km/s (24 eV), 7.25 km/s (43.5 eV), and 10.04 km/s (83.5 eV) incident velocities (energies) are shown in Figure 4.6. Clearly, the maximum yield occurs for backscattered products at  $0^\circ$  exit angle, and the yield continually decreases as the products scatter off-normal. Consistent with the polar intensity plots obtained for the atomic projectiles, the widths of the distributions are obtained by fitting the data to equation 3.4 and calculating the FWHM according to equation 3.5.

Interestingly, Figure 4.7 demonstrates the unique relationship between the FWHM for the two products calculated as a function of the  $\text{Br}_2^+$  collision velocity. The FWHM values calculated for incident  $\text{Br}^+(\text{}^3P_2)$  are overlaid on the plot for future comparisons. Across the range of incident velocities explored, the  $\text{Br}^-$  fragments leave the surface with a broader distribution compared to the emerging  $\text{Br}_2^-$  products. A comparison to the yield data shown in Fig. 4.4 reveals that the scattered products leave the surface with the narrowest angular distributions coincident with the resonance feature near 7.5 km/s collision velocity. This trend suggests that trajectories responsible for the enhanced negative ion formation and scattered kinetic energy near the resonance also result in the narrowest angular distributions. Even more intriguing is the tracking behavior of the scattered  $\text{Br}^-$  products with the  $\text{Br}_2^-$

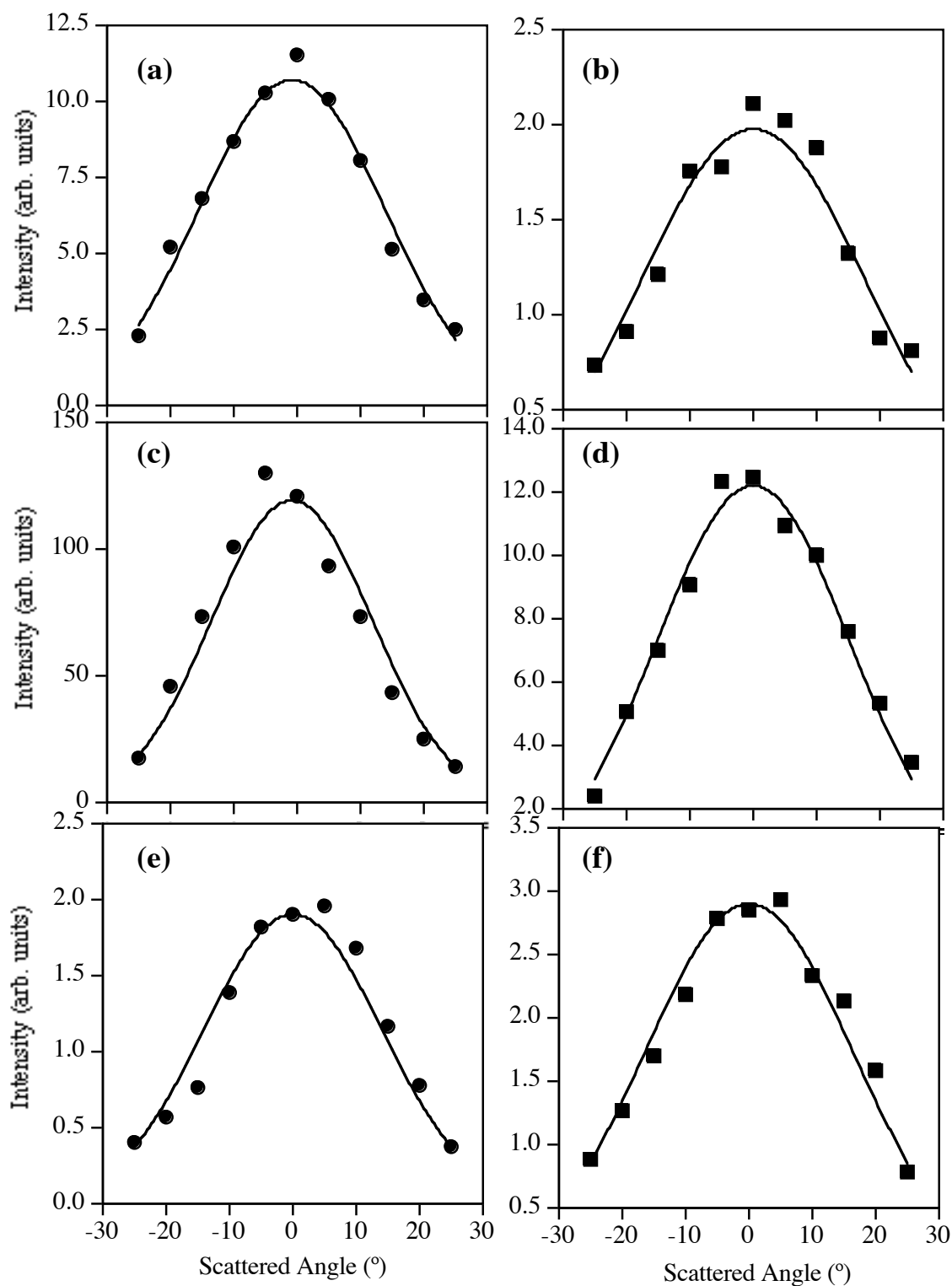


Figure 4.6. The  $\text{Br}_2^-$  (a, c, and e) and  $\text{Br}^-$  (b, d, and f) product intensities versus scattering angle for  $\text{Br}_2^+$  collision energies (a and b) 24 eV, (c and d) 43.5 eV, and (e and f) 83.5 eV. The solid curves represent the results from fitting the data to equation 3.4.

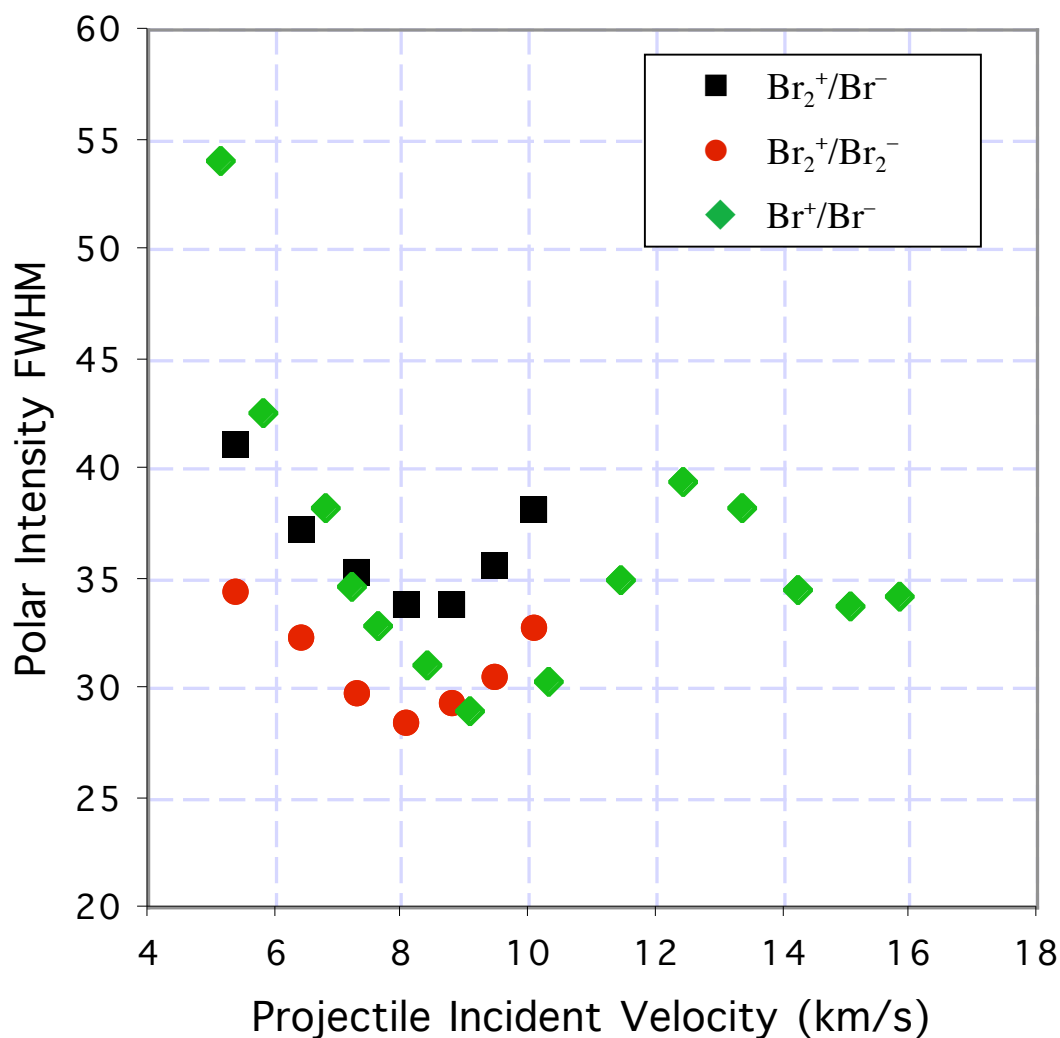


Figure 4.7. The FWHM values calculated from the best curve fits to the polar intensity distributions of scattered  $\text{Br}_2^-$  and  $\text{Br}^-$  as a function of the  $\text{Br}_2^+(\text{}^2\Pi_{g3/2}, \nu=0)$  collision velocity at  $T_s = 25^\circ \text{C}$ . The FWHM values calculated from the polar intensity data for scattering  $\text{Br}^+(\text{}^3P_2)$  on Pt(111) is overlaid on the plot for comparison.



products. Regardless of the  $\text{Br}_2^+$  velocity, the ratio of the FWHM values for each product is constant. This unexpected behavior suggests that the mechanisms responsible for the emergence of  $\text{Br}^-$  and  $\text{Br}_2^-$  are related to each other.

#### 4.3.2. Reaction Dynamics: Role of Translational Energy

Across the translational energy regime explored (24 - 84 eV), collisions of  $\text{Br}_2^+(^2\Pi_{g3/2}, v=0)$  molecules with Pt(111) result in the emergence of two negative ions,  $\text{Br}_2^-$  and  $\text{Br}^-$ . The survival probability for  $\text{Br}_2^+$  scattering from the surface across the same energy range is less than  $10^{-6}$ , suggesting a very efficient neutralization process for the incident molecular ions. Although several excited states for  $\text{Br}_2^-$  exist, only molecular anions in the ground electronic state,  $^2\Pi_u^+$ , are likely to emerge from the surface. The remaining seven identified  $\text{Br}_2^-$  excited states are either very weakly bound ( $D_0 < 0.2$  eV) or dissociative.<sup>3</sup> For the formation of  $\text{Br}^-$ , only the ground electronic state,  $^1S_0$ , is stable against autodetachment. Therefore, these scattering experiments resolve the state-to-state transformations of  $\text{Br}_2^+(^2\Pi_{g3/2}, v=0)$  to  $\text{Br}_2^-(^2\Pi_u^+)$  and  $\text{Br}^-(^1S_0)$  on Pt(111). The formation of both anionic products involves the transfer of two electrons from the surface to the scattered products. In addition, the emergence of  $\text{Br}^-(^1S_0)$  products requires the parent bromine molecule to dissociate either before, during, or after collision with the surface.

Several experiments involving hyperthermal energy collisions of diatomic molecules with surfaces have revealed that neutralization is very facile before collision with the surface.<sup>8,9</sup> An electron, that transfers from the surface to  $\text{Br}_2^+$  on the inbound trajectory, can populate ground ( $X\ ^1\Pi_g^+$ ), excited ( $A\ ^3\Pi_u, B\ ^3\Pi_u$ ), or even repulsive ( $C\ ^1\Pi_u$ ) electronic states of the bromine molecule as illustrated in Figure 4.8. When the ionization potential is corrected for image charge shifts within 5 Å of

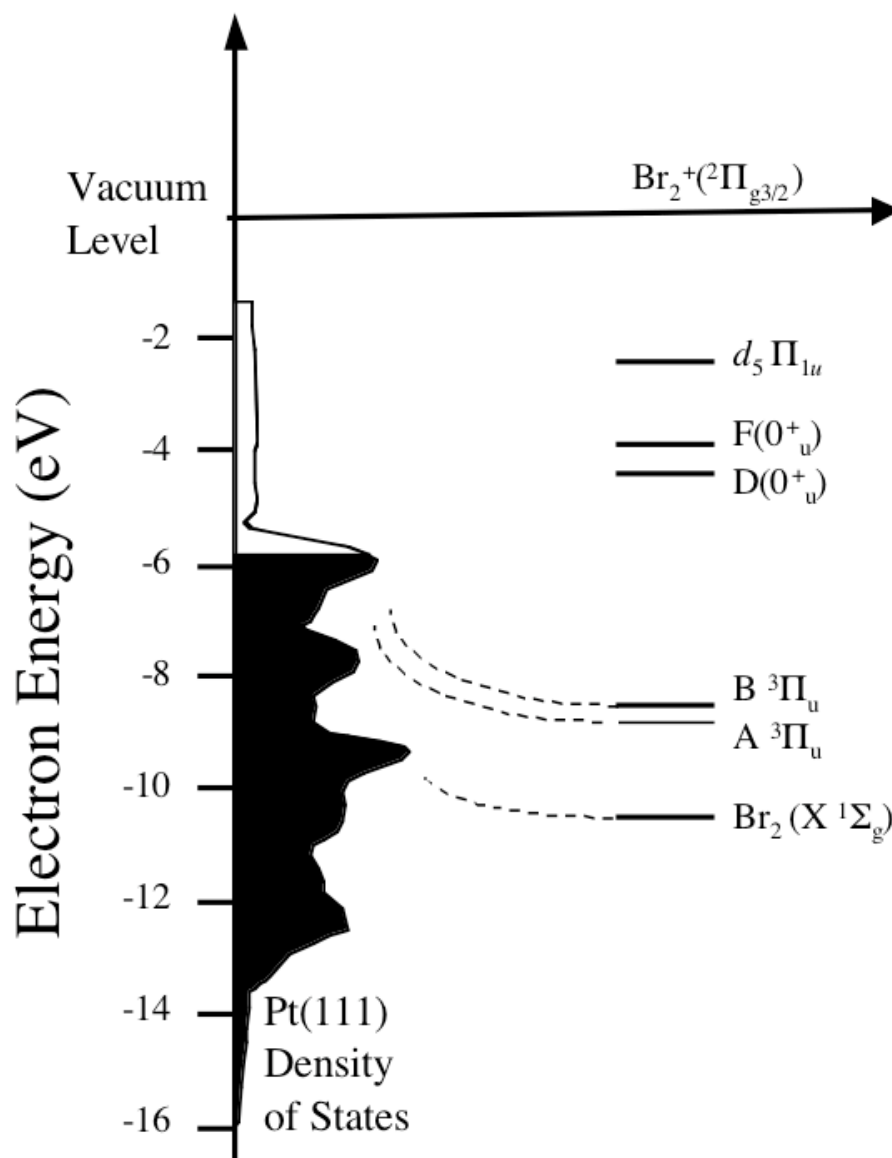


Figure 4.8. One-electron energy level diagram depicting neutralization of  $\text{Br}_2^+(^2\Pi_{g3/2})$  near Pt(111). The density of states for Pt(111) as calculated by Kokalj and Causa<sup>10</sup> is shown on the left, where the occupied states are shaded. The energy levels corresponding to the neutral bromine electronic states are obtained from various literature sources.<sup>2-4,11</sup> The dashed curves indicate the energy shift of the electronic states as the molecule approaches the Pt(111) surface.

the surface (Fig. 4.8), the ground and first two excited states are still degenerate with the occupied electronic states for Pt(111). Due to the significantly greater yield of  $\text{Br}_2^-$  compared to  $\text{Br}^-$ , it is reasonable to suggest that the majority of incident projectiles are neutralized into the ground electronic state before collision with the surface.

If an electron from the surface transfers to the  $A^3\Pi_u$ ,  $B^3\Pi_u$  or  $C^1\Pi_u$  excited electronic states of  $\text{Br}_2$  on the inbound trajectory, then the incident molecule will probably dissociate before colliding with the surface, because of the low dissociation energy within these states. The resulting fragments will be formed exclusively in the  $^2P_{3/2}$  state if the  $A$  state is populated, or in either the  $^2P_{3/2}$  or the  $^2P_{1/2}$  state if the  $B$  state is populated. The bromine fragments will impact the surface as separate atoms and can capture a second electron from the surface to emerge exclusively as  $\text{Br}^-(^1S_0)$ .

If this dissociative neutralization mechanism is operative for the  $\text{Br}_2^+/\text{Pt}(111)$  system, then the scattering distribution for  $\text{Br}^-(^1S_0)$  fragments is expected to be similar to that measured when  $\text{Br}^+$  scatters on the same surface and emerges as  $\text{Br}^-(^1S_0)$ . Figure 4.5 shows that for all the bromine collision velocities utilized in this study, the scattered  $\text{Br}^-$  products leave the surface with comparable exit velocities, independent of whether  $\text{Br}^+$  or  $\text{Br}_2^+$  is the incident projectile. This behavior is consistent with a DN mechanism. However, for the same collision velocities the shapes of the  $\text{Br}^-(^1S_0)$  velocity distributions should also be similar. Figure 4.9 compares the scattered  $\text{Br}^-(^1S_0)$  velocity distributions for  $\text{Br}_2^+(^2\Pi_{g3/2})$  and  $\text{Br}^+(^3P_2)$  at several comparable collision velocities. The horizontal axis represents the ratio of the exit velocity to the incident velocity to account for slight differences in the collision velocities of the two incident projectiles. For collision velocities at 7.2 km/s or less, the  $\text{Br}^-(^1S_0)$  velocity distributions are found to be identical within experimental uncertainty. For higher incident velocities, the  $\text{Br}^-(^1S_0)$  products that result from  $\text{Br}^+(^3P_2)$  collisions leave the surface at higher velocities compared to  $\text{Br}^-(^1S_0)$  originating from the molecular

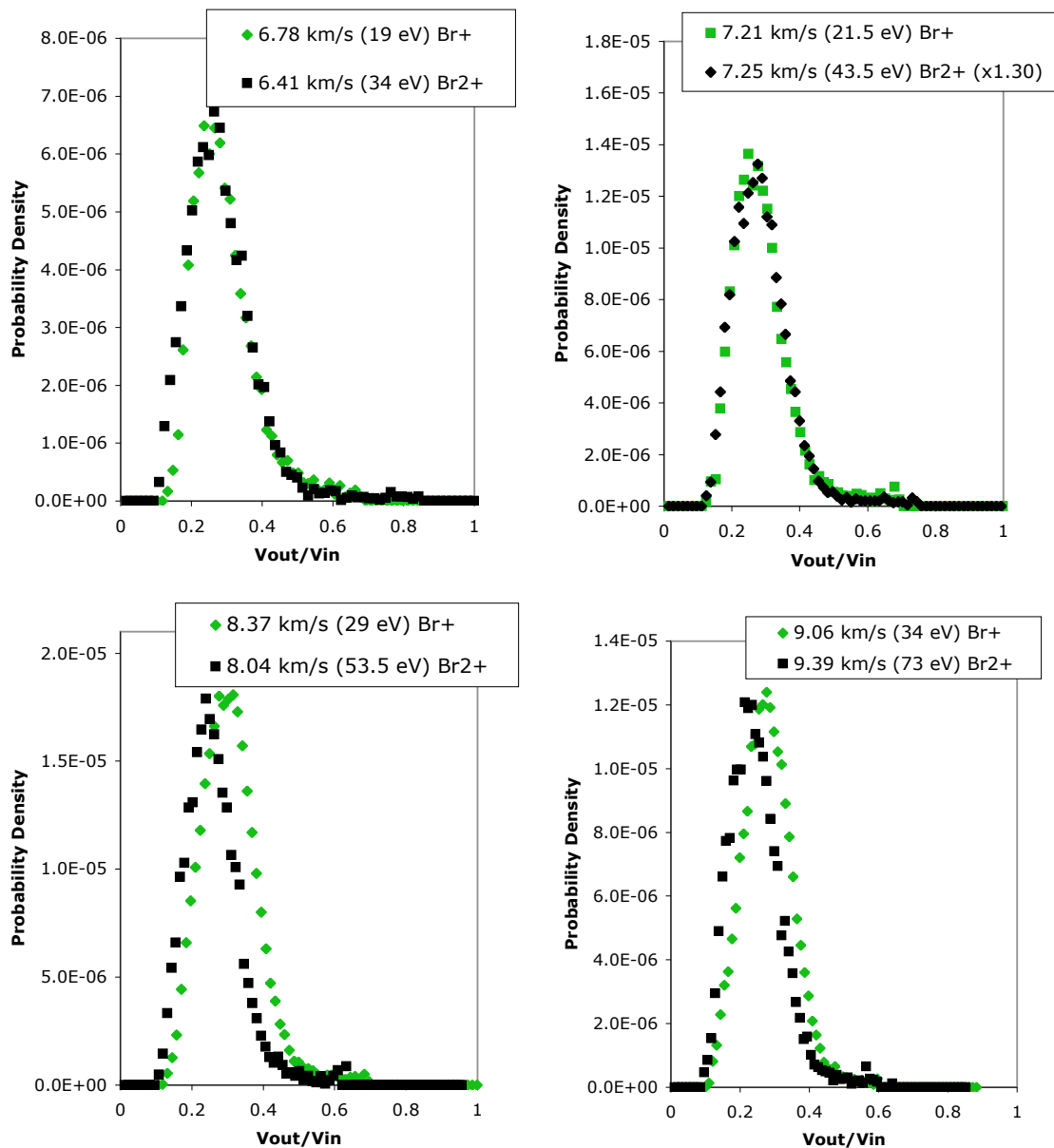


Figure 4.9.  $\text{Br}^-$  velocity distributions resulting from  $\text{Br}_2^+(^2\Pi_{g3/2}, v=0)$  and  $\text{Br}^+(^3P_2)$  projectiles, incident at the specified velocities. The probability density for the  $\text{Br}_2^+(^2\Pi_{g3/2}, v=0)$  projectile is rescaled so that the two distributions can be readily compared.

projectiles. This behavior suggests that DN is most likely to occur for incident velocities at or below 7.2 km/s for the  $\text{Br}_2^+/\text{Pt}(111)$  system.

Previous experiments have shown that the DN mechanism is very sensitive to the collision velocity.<sup>12</sup> When the projectile approaches the surface slowly, the molecule has sufficient time to dissociate before colliding with the surface. Figure 4.10 illustrates the bond length for  $\text{Br}_2(A^3\Pi_u)$  as a function of the distance,  $Z$ , between the projectile and the surface calculated at three collision energies using the Ziegler-Biersack-Littmark (ZBL) and image charge potentials.<sup>13</sup> A 20 eV incident  $\text{Br}_2^+$  ion that neutralizes to the excited  $\text{Br}_2(A^3\Pi_u)$  state 5 Å in front of the surface will have enough time to separate more than 1.25 Å beyond the 2.75 Å equilibrium bond length prior to colliding with the surface. When the collision energy increases to 80 eV, the molecule only has enough time for the bond length to stretch from 2.75 Å to 3 Å—not enough time to fragment before the collision. Therefore, the largest number of  $\text{Br}^-$  fragments would be expected to emerge at the lowest collision energies. However, the probability that the electron is lost back to the surface along the exit trajectory decreases with increasing exit velocity. Consequently, the dependence of the  $\text{Br}^-$  yield on collision velocity is expected to exhibit a maximum value due to the competing processes in a DN mechanism.

Neutralization to the dissociative states is not as efficient as neutralization to the ground state of the bromine molecule as evidenced by the larger yield of  $\text{Br}_2^-$  compared to  $\text{Br}^-$ . Since electrons from the surface preferentially occupy the ground  $\text{Br}_2(X^1\Pi_u^+)$  state on the inbound trajectory, it is worthwhile to consider a dissociation mechanism that occurs after the collision with the surface. In delayed SID of polyatomic molecules, excitation of the molecular vibrations results from the impact with the surface, inducing a postcollision unimolecular dissociation.<sup>12</sup> This mechanism implies that the bromine molecule dissociates on the exit trajectory at a distance from the surface that is too far for the fragments to capture electrons from

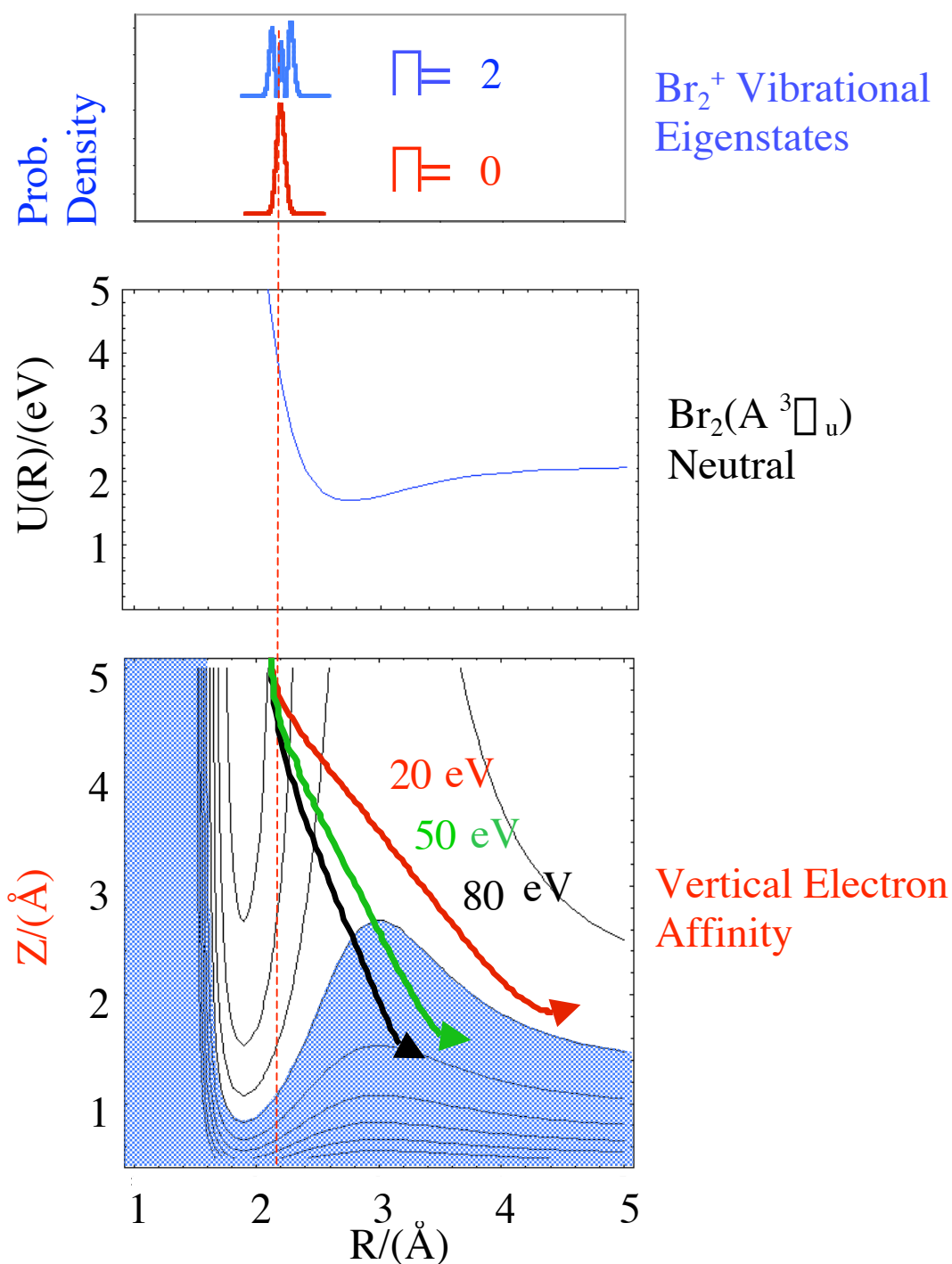


Figure 4.10. Ziegler-Biersack-Littmark (ZBL)<sup>13</sup> trajectory calculations for  $\text{Br}_2^+(^2\Pi_{g3/2}, \nu=0)$  neutralized to the  $\text{Br}_2(\text{A } ^3\Pi_u)$  state prior to colliding with Pt(111) surface. The equilibrium bond distance for  $\text{Br}_2(\text{A } ^3\Pi_u)$  state is 2.75 Å.

Pt(111). Within this scenario,  $\text{Br}_2^-$  molecules would have to be formed close to the surface, then dissociate into negative and neutral Br fragments. The fragments are expected to leave the surface with the same average velocities as the parent  $\text{Br}_2^-$ . The data in Figs. 4.3 and 4.5 reveal that the  $\text{Br}^-$  fragments emerge from the surface with a higher velocity than the  $\text{Br}_2^-$  products, and that the difference in velocity increases with increasing collision energy. Furthermore, delayed SID has only been implicated in collisions of polyatomic molecules, where the impulsive transfer of kinetic energy to the projectile is redistributed across several vibrational modes, until a particular mode gains sufficient energy to induce dissociation. Therefore, it is implausible for  $\text{Br}^-$  emergence to arise from delayed SID of  $\text{Br}_2$  or  $\text{Br}_2^-$ . If impulsive dissociation occurs, then the fragments must separate while in close proximity to the surface.

Neutralization of  $\text{Br}_2^+(\text{}^2\Pi_{g3/2}, v=0)$  followed by a second electron transfer into a dissociative state of  $\text{Br}_2^-$  can potentially lead to scattered  $\text{Br}^-(^1S_0)$  fragments. Kurepa *et al.*<sup>2</sup> detected six different dissociative attachment processes for gas-phase bromine molecules. If the  $\text{Br}^-(^1S_0)$  products observed in the current experiments are formed through a  $\text{Br}_2^-$  excited state intermediate, electron transfer to the dissociative state is expected to increase with increasing collision velocity. Competitive to the electron capture process is the electron loss process as the molecule leaves the surface. Since the survival probability for negative ions increases with increasing projectile velocity, the  $\text{Br}^-$  yield will exhibit a maximum value. Moreover, the emerging  $\text{Br}^-(^1S_0)$  will exit the surface at velocities comparable to the  $\text{Br}_2$  parent molecule if dissociation proceeds after impact. Figures 4.3 and 4.5 reveal that  $\text{Br}_2^-$  and  $\text{Br}^-$  scatter from the surface with significantly different exit velocities when  $\text{Br}_2^+$  velocities exceed 7.2 km/s. Therefore, the DA mechanism is not operative for collision velocities above 7.2 km/s, but may contribute to the formation of  $\text{Br}^-$  at lower incident velocities.

Although electronic transitions between the surface and projectile are sufficient to explain the dissociation mechanism for collision velocities below 7.2 km/s, these

mechanisms fail to predict the dynamics observed for higher  $\text{Br}_2^+$  incident velocities. Instead, a collision induced dissociation mechanism that occurs in close proximity to the surface may contribute to the formation of  $\text{Br}^-$ . Dissociation occurs as a result of an impulsive transfer of incident translational energy to rovibrational energy. A comparison of the amounts of time required for half a vibrational period of  $\text{Br}_2$  ( $5 \times 10^{-14}$  s) and for  $\text{Br}_2$  to travel 3 Å away from the surface ( $1.5 \times 10^{-13}$  s traveling at 2.0 km/s) indicates that the neutralized molecule has sufficient time to dissociate before escaping the surface. The neutral atomic fragments have some probability then to capture electrons along the exit trajectory to form  $\text{Br}^-(^1S_0)$ . The fragments formed through this rapid mechanical dissociation are expected to emerge with a greater velocity compared to the exit velocity of the parent projectile.<sup>8,12</sup> Figure 4.5 shows that indeed the bromine fragment emerges from the surface with greater kinetic energy than its molecular precursor across the range of incident velocities. The velocity difference between the  $\text{Br}_2^-$  and  $\text{Br}^-$  products continually increases with increasing incident velocity above 7.2 km/s, as more energy is released in the impulsive dissociation of the fragments.

The collision energy threshold value for the emergence of dissociated products provides important information about the dissociation mechanism. A signature of the CID mechanism is a translational energy threshold for fragmentation that exceeds the reaction endoergicity by a factor of 4-5. In contrast, relatively low thresholds suggest a DN mechanism.<sup>12</sup> The open squares in Figure 4.4 represent the  $\text{Br}^-$  yield for  $\text{Br}_2^+(^2\Pi_{g3/2}, v=0)$  incident on Pt(111). The results reveal a  $\text{Br}^-(^1S_0)$  threshold value between 3.0 km/s (7.5 eV) and 3.4 km/s (9.5 eV). The bond dissociation energy for  $\text{Br}_2$  is 2.0 eV, which is approximately 1/4 the observed threshold energy. Therefore, the threshold value near 8.5 eV is consistent with a CID mechanism or with DN followed by electron attachment.



The distribution of exit angles for the scattered products provides additional insight into the detailed dynamics. The FWHM of the angular distributions observed for both product channels in Fig. 4.7 is similar to the FWHM of the  $\text{Br}^-(^1S_0)$  angular distribution obtained for  $\text{Br}^+$  scattered on Pt(111). In all cases, the narrowest angular distributions occur coincident with the maximum yield values (Fig. 4.4). This similarity between the data suggests that the scattered products are very sensitive to the surface impact site—atop, bridge, or three-fold hollow—with the narrowest angular distributions occurring for trajectories that impact the three-fold hollow sites. For a CID dissociation mechanism, the bromine fragments will scatter into a broader angular distribution than that of the parent molecules, because of the momentum of the separating fragments. Similar behavior is expected for DN, because the fragments only have enough time to separate by 5 Å, at most, before the atoms collide with the surface.

The reaction dynamics for the emergence of  $\text{Br}_2^-$  from  $\text{Br}_2^+$  projectiles are very similar to the behaviors observed in Chapter 3 for the formation of  $\text{Br}^-$  from incident  $\text{Br}^+$ . Both experiments reveal an unprecedented resonance feature with a very narrow FWHM for the yield dependence on the incident energy. Coincident with the resonance features, the products emerge from the surface with additional kinetic energy and with the narrowest angular distributions. As with the atomic projectile, the emergence of molecular bromine anions is extremely sensitive to the impact site (i.e. atop, bridge, or three-fold hollow) on the Pt(111) surface. The displacements of the platinum atoms at the point of impact as well as the surrounding Pt atoms are expected to depend on the particular collision site. The deformation created in the surface transiently modifies the electronic coupling between the projectile and the surface in a manner that causes very efficient electron transfer for particular collision energies. Trajectories that scatter from atop or bridge sites should result in

significantly less efficient electron transfer from the surface to the projectile due to the different displacement of the surface atoms.

Overall, the reaction dynamics for scattering  $\text{Br}_2^+(^2\Sigma_{g3/2}^-, v=0)$  on Pt(111) is quite complex. The incident molecular ions neutralize predominantly to the  $\text{Br}_2(\text{X } ^1\Sigma_u^+)$  ground electronic state. A second electron is transferred from the surface to the neutral molecule to form  $\text{Br}_2^-(^2\Sigma_u^+)$ . The resonance feature is assigned to a trajectory dependent mechanism that depends on the electronic coupling between the transient motion of the surface atoms and the scattered products. The emergence of  $\text{Br}^-$  is most likely due to the combination of DN and CID, where DN dominates at collision velocities below 7.2 km/s, and CID is more efficient at higher collision velocities.

### 4.3.3 Reaction Dynamics: Role of Surface Temperature

An intriguing surface temperature dependence on the negative ion formation was observed for state-selected bromine atoms scattered from Pt(111) (see Sect. 3.3.5). When the surface temperature increased from 25° C to 400° C the maximum intensity of the negative ion formation decreased and the peak of the resonance feature shifted by 0.6 eV to a lower collision energy. This unexpected behavior was attributed to an increase in the vibrational energy of the surface atoms at higher temperatures, which modifies the transient electronic coupling between the surface and the scattering bromine atomic projectiles. In order to investigate the generality of this unusual behavior,  $\text{Br}_2^+(\text{}^2\Pi_{g3/2}, v=0)$  ions are scattered on a 400° C Pt(111) surface and the results are compared to scattering on a room temperature surface.

In order to minimize experimental errors, the  $\text{Br}_2^+(\text{}^2\Pi_{g3/2}, v=0)$  scattering experiments at a given incident energy are performed on the room temperature and the 400° C surface on the same day. For each collision energy, the ratio of the product yield at 400° C to the product yield at 25° C is calculated. Figure 4.11 illustrates the effect of the surface temperature on the formation of  $\text{Br}_2^-$  and  $\text{Br}^-(^1S_0)$  across the 24 to 84 eV  $\text{Br}_2^+$  collision energy range. Similar to the trend observed for scattering atomic ions on Pt(111), the product yield ratios are almost linearly dependent on the collision energy, where the greatest  $\text{Br}^-$  and  $\text{Br}_2^-$  enhancement occurs at 24 eV and the largest negative ion inhibition occurs near 84 eV. Surprisingly, the yield ratios for both scattered products are equal within experimental error at every incident energy.

To better understand the yield ratio data, the product yields at each surface temperature are plotted versus the  $\text{Br}_2^+(\text{}^2\Pi_{g3/2}, v=0)$  kinetic energy in Fig. 4.12. The linear dependence of the yield ratio on collision energy correlates to a slight energy shift in the resonance position for both scattered products. To quantify this energy

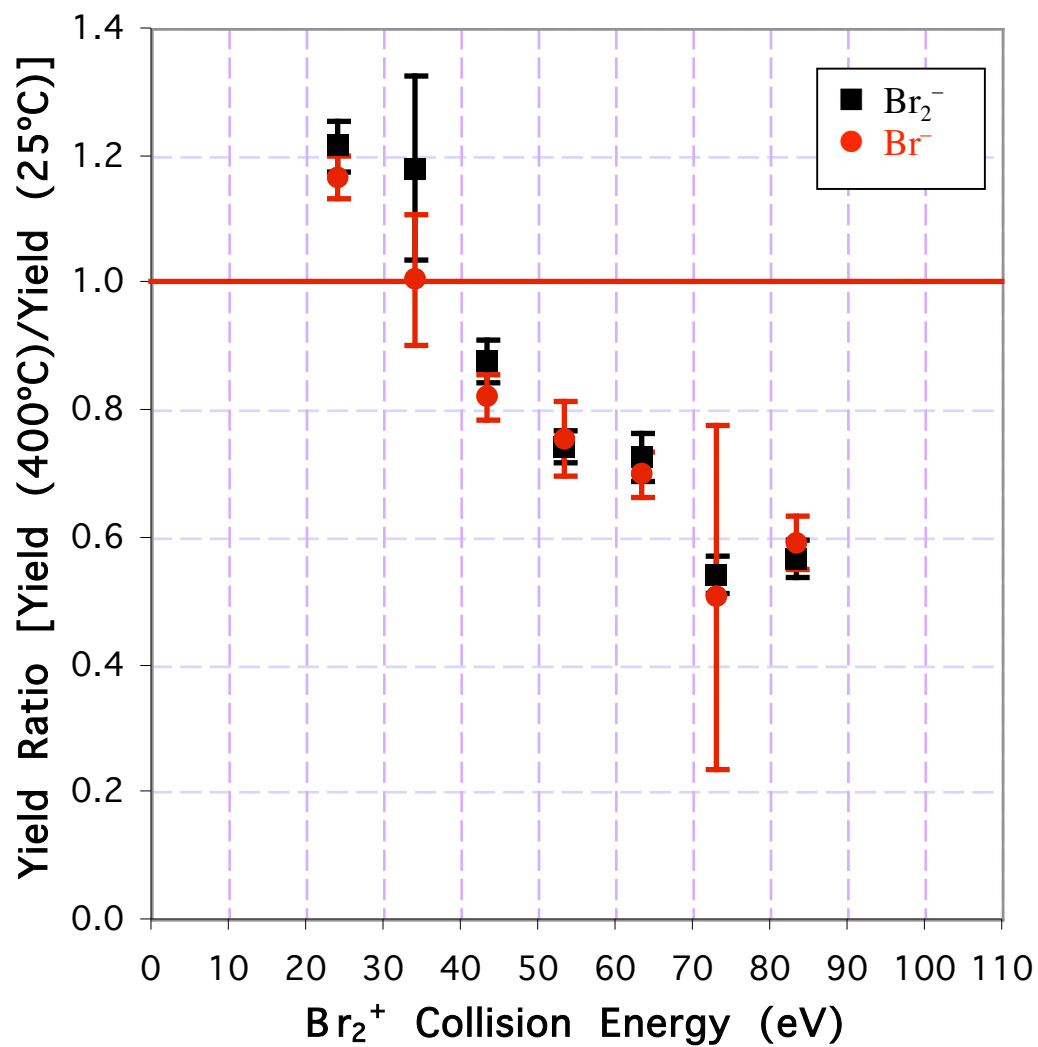


Figure 4.11. Ratio of the Br<sub>2</sub><sup>-</sup> and Br<sup>-</sup> product yield values at T<sub>s</sub> = 400° C to the yield values at T<sub>s</sub> = 25° C as a function of the incident Br<sub>2</sub><sup>+</sup>(<sup>2</sup>Π<sub>g3/2</sub>, ν = 0) collision energy. A ratio value equal to one indicates no temperature effect.

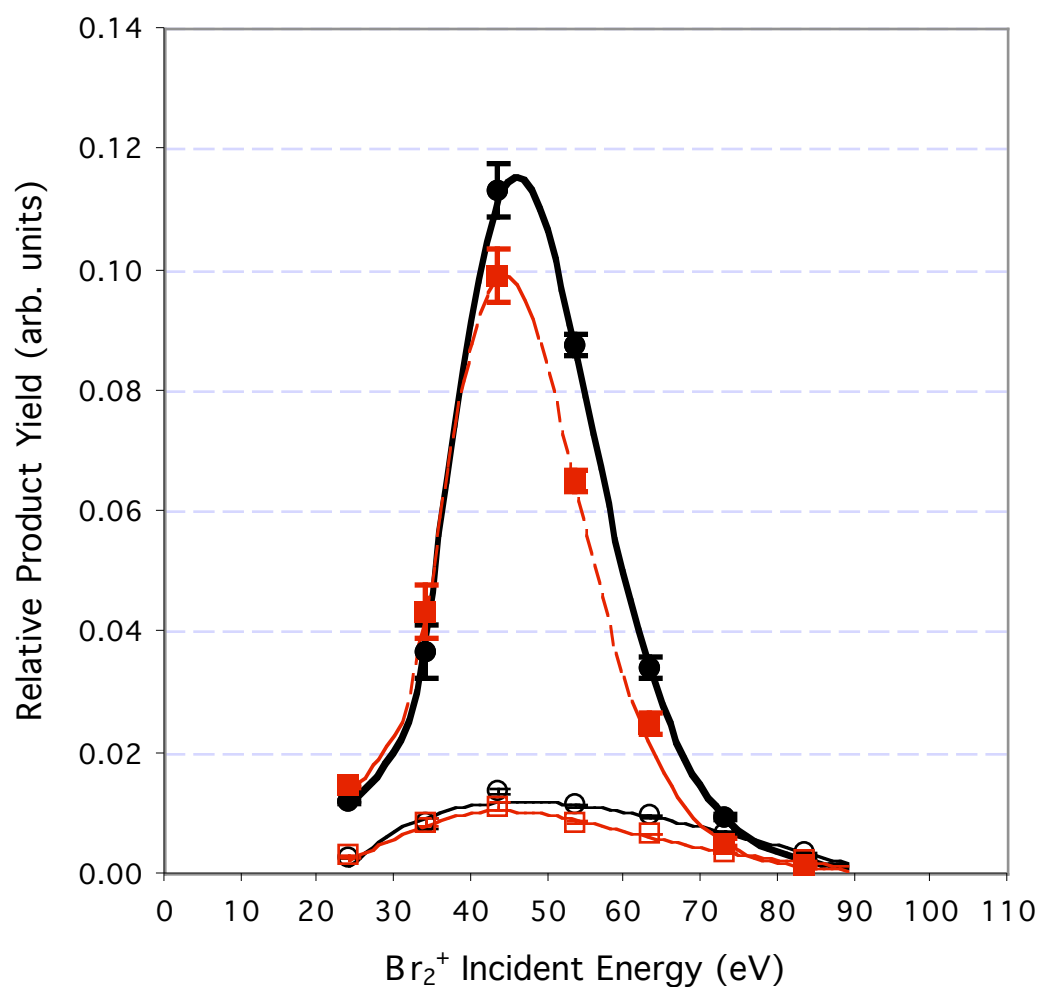


Figure 4.12. Br<sub>2</sub><sup>-</sup> and Br<sup>-</sup> product yields at T<sub>s</sub> = 25° C and 400° C as a function of the incident Br<sub>2</sub><sup>+</sup>(<sup>2</sup>Π<sub>g3/2</sub>, ν=0) collision energy. The lines represent the best fit to the yield data.

shift, the yield data corresponding to the 34-84 eV  $\text{Br}_2^+$  collision energy range are fit to the lognormal function (Eq. 3.12) utilizing the Igor curve fitting program.<sup>14</sup> The best curve fits are obtained when the experimental error bars (90% confidence) are included in the Igor curve fitting analysis. Table 4.2 summarizes the best fitting parameters with the corresponding 90% confidence limits for the  $\text{Br}_2^-$  and  $\text{Br}^-$  yield data collected at  $T_s = 25^\circ\text{C}$  and  $400^\circ\text{C}$ . These curve fits reveal that the  $\text{Br}_2^-$  and  $\text{Br}^-$  resonance peak shifts by  $1.8 \pm 0.5$  eV and  $2.7 \pm 1.8$  eV, respectively, to lower collision energies when the temperature of the surface is increased from  $25^\circ$  to  $400^\circ\text{C}$ . Moreover, when  $\text{Br}_2^+$  is scattered on the  $400^\circ\text{C}$  surface, the negative ion intensity significantly decreases at the peak position of the resonance feature for both scattered products, as determined by comparing the  $A$  fitting parameters at the two surface temperatures.

TABLE 4.2 IGOR CURVE FITTING-BEST FITTING-PARAMETERS FOR  $\text{Br}_2^-$  AND  $\text{Br}^-$  YIELD

Product	Fitting Parameters	$T_s=25^\circ\text{C}$	Error Bars (90% Confidence)	$T_s=400^\circ\text{C}$	Error Bars (90% Confidence)
$\text{Br}_2^-$	$y_0$	0.00036	$\pm 3.6\text{E-}04$	0.00038	$\pm 4.5\text{E-}05$
	$A$	0.115	$\pm 3.8\text{E-}03$	0.099	$\pm 2.5\text{E-}04$
	$E_0$	46.05	$\pm 0.45$	44.27	$\pm 0.060$
	$w$	0.29	$\pm 0.009$	0.29	$\pm 0.001$
	$r^2$	0.99		0.98	
$\text{Br}^-$	$y_0$	-0.094	$\pm 0.34$	-3.3E-04	$\pm 0.0013$
	$A$	0.106	$\pm 0.34$	0.011	$\pm 0.0012$
	$E_0$	46.57	$\pm 1.57$	43.84	$\pm 0.79$
	$w$	2.03	$\pm 3.39$	0.51	$\pm 0.07$
	$r^2$	0.98		0.95	

The changes in the scattering dynamics with surface temperature result from modifications to the surface properties. Since the formation of negative ions depends on a resonance between the molecular states and the occupied electronic states of the surface, one might expect that the charge transfer dynamics are altered by a change in the work function. However, the 375° increase in the surface temperature only corresponds to ~0.056 eV decrease in the work function of the surface, which is significantly lower than the energy shift observed in the peak position of the resonance features. Moreover, a decrease in the work function would result in a more efficient electron transfer process, corresponding to a yield ratio value greater than 1.0 across the entire incident energy range. Figure 4.11 shows the yield ratio value is extremely sensitive to the collision energy, suggesting that the work function changes in the surface is not sufficient to explain the intriguing temperature effects.

An increase in the surface temperature also causes an increase in the vibrational motion of the surface atoms. This additional motion translates to a  $3kT$  increase in the vibrational energy for each surface atom. For the Pt(111) surface, this corresponds to a 0.097 eV increase in vibrational energy per surface atom when the surface temperature is increased from 25° C to 400° C. When a bromine molecule collides with the surface, it can interact with several Pt atoms, depending on the orientation of the molecule and impact parameter. The combined vibrational energy for the surface atoms at the impact site can range between 0.097 eV to more than 0.97 eV, which is the same order of magnitude as the  $1.8 \pm 0.5$  and  $2.7 \pm 1.8$  eV resonance shift for the  $\text{Br}_2^-$  and  $\text{Br}^-$  products, respectively. Detailed classical trajectory calculations are necessary to determine the average number of surface atoms that interact with the bromine projectiles.

Can this increased vibrational motion explain the inhibition in the negative ion formation at the peak of the resonance? When the incident projectile impacts the surface, the electronic coupling between the surface and the projectile is modified due

to the transient deformation of the surface as described in Section 4.3.2. An increase in the vibrational motion of the surface atoms disturbs the phasing between the motion of the surface atoms at the point of impact in such a manner that decreases the emergence of negative ions. The phasing between the motion of the products and the surface atoms is critical to the charge transfer resonance observed of both the  $\text{Br}_2^-$  and  $\text{Br}^-$  products.

#### 4.3.4 Reaction Dynamics: Role of Initial Vibrational Energy

Additional experiments are performed to investigate the effect of the incident projectile's vibrational energy on the reaction dynamics. In these experiments,  $\text{Br}_2^+(\text{}^2\Pi_{g3/2}, \nu)$  is scattered on room temperature Pt(111), and the  $\text{Br}_2^-$  and  $\text{Br}^-$  product yields and kinetic energies are measured as a function of the collision energy. In order to make a direct comparison of the experimental results for the two incident vibrational states, the data for the same  $\text{Br}_2^+(\text{}^2\Pi_{g3/2}, \nu)$  incident energy are alternately collected for  $\text{Br}_2^+(\nu=0)$  and  $\text{Br}_2^+(\nu=2)$  on the same day using a comparable number of incident ions. The experiments for scattering  $\text{Br}_2^+$  ions with a specific translational energy are repeated on four different days to confirm the overall vibrational effect.

Figure 4.13 shows the ratios of the  $\text{Br}_2^-$  and  $\text{Br}^-$  product yields for  $\text{Br}_2^+$  ions prepared in the  $\nu=2$  to  $\nu=0$  states as a function of the  $\text{Br}_2^+(\text{}^2\Pi_{g3/2}, \nu)$  translational energy. A yield ratio value equal to 1.0 indicates that negative ion formation is independent of the vibrational state of the incident projectile. Within the error bars, the formation of  $\text{Br}_2^-$  does not significantly depend on the initial vibrational state across the incident energy range explored. However, the formation of  $\text{Br}^-$  *does* depend on the vibrational energy of the  $\text{Br}_2^+$  molecules for incident translational energies below 30 eV. In fact, as the collision energy decreases below 30 eV, the



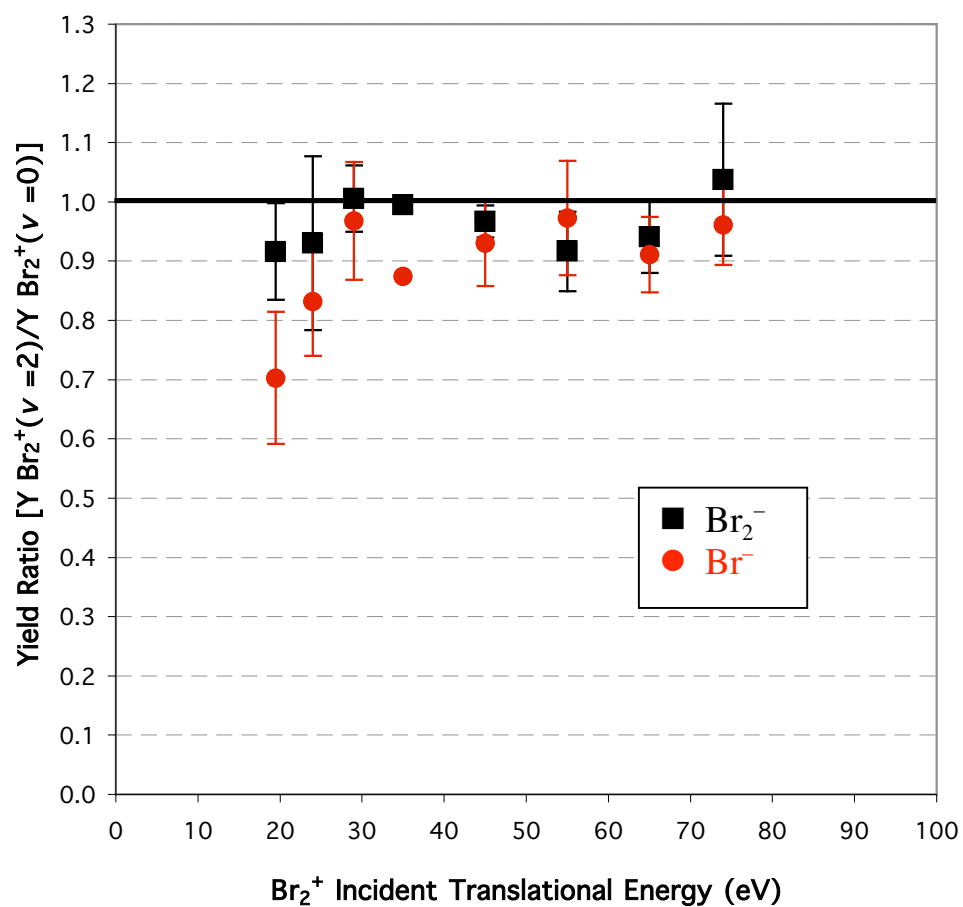


Figure 4.13. The average ratios of the Br<sub>2</sub><sup>-</sup> and Br<sup>-</sup> product yields for scattering Br<sub>2</sub><sup>+</sup>(<sup>2</sup>g<sub>3/2</sub>, v) in v=2 to v=0 on Pt(111). The Br<sub>2</sub><sup>+</sup> translational energy spans from 19.5 eV and 73.5 eV while the Pt(111) surface is held at room temperature. The horizontal line at 1.0 represents the absence of a vibrational effect on negative ion formation.

negative ion formation for the dissociated fragments becomes less efficient if the incident molecule is formed in the  $v=2$  vibrational state. Surprisingly, this behavior is opposite to the trend observed by Martin et. al, where an increase in the  $\text{NO}^+(\text{X } ^1\Sigma^+, v)$  vibrational quanta enhanced the probability to form dissociated  $\text{O}^-$  products.<sup>8</sup>

In addition to measuring the probability for negative ion formation, the data analysis also allows one to obtain the final kinetic energy of the scattered products. The  $\text{Br}_2^-$  and  $\text{Br}^-$  final kinetic energies are measured as a function of the  $\text{Br}_2^+$  incident translational energy. Figure 4.14 compares the final kinetic energies of the products for  $\text{Br}_2^+$  molecules prepared in the  $v=0$  and  $v=2$  vibrational states. Within the experimental error bars, the additional vibrational energy in the incident projectile does not significantly affect the final kinetic energies of the emerging products. This is not surprising, since the internal energy difference for the incident projectile prepared in the  $v=0$  and  $v=2$  vibrational states is only 0.09 eV.

In order to explain the intriguing vibrational effect on the  $\text{Br}^-$  yield, one must return to the mechanisms assigned to the formation of the two products described in Section 4.3.2. The emergence of  $\text{Br}_2^-$  requires a sequential two-electron transfer process, where the incident projectile neutralizes to the ground electronic state followed by a second electron transfer to the  $\text{Br}_2^-(^2\Sigma_u^+)$  state on the exit trajectory. Two dissociation mechanisms are considered for the emergence of  $\text{Br}^-(^1S_0)$ ; DN for low  $\text{Br}_2^+$  translational energies (below 44 eV) and CID for higher incident energies. If CID is the operative mechanism, then a slight enhancement in the product dissociation yield would be expected for higher incident vibrational quanta.<sup>15</sup> The data suggest that CID is not the dominant dissociation channel responsible for the formation of  $\text{Br}^-$  at collision energies below 44 eV.

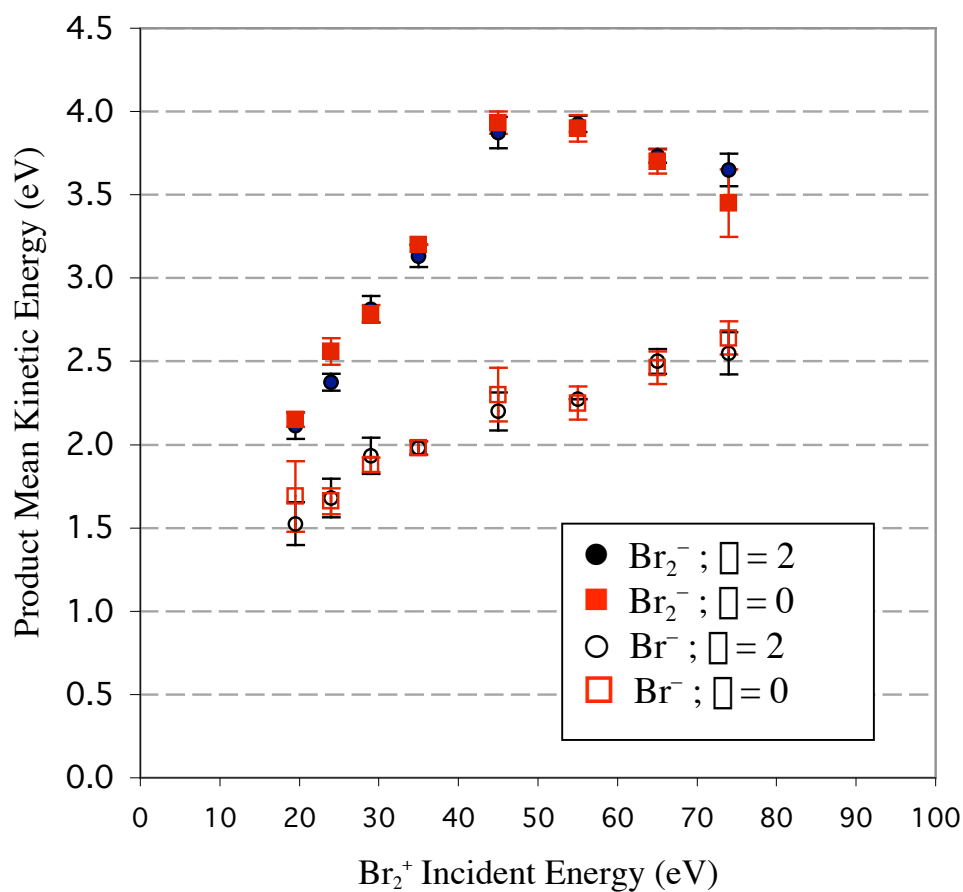


Figure 4.14. A comparison of the translational energies of the emerging Br<sub>2</sub><sup>-</sup> and Br<sup>-</sup>(<sup>1</sup>S<sub>0</sub>) products versus the Br<sub>2</sub><sup>+</sup>(<sup>2</sup>Π<sub>g3/2</sub>, *v*) incident kinetic energy scattering from a room temperature Pt(111) surface. The squares and circles represent the products resulting from incident projectiles prepared in the *v* = 0 and *v* = 2 states, respectively.

Instead, the neutralization of the incident  $\text{Br}_2^+(^2\Pi_{g3/2}, \nu)$  molecule moderates the vibrational effect observed in the scattering data. When the incident projectile neutralizes to the ground electronic state of  $\text{Br}_2(X^3\Pi_u)$ , the probability for neutralization is independent of the initial vibrational state as illustrated in Figure 4.15. The top panel shows the  $\text{Br}_2^+$  vibrational eigenstates for  $\nu = 0$  and  $\nu = 2$  as calculated by the LEVEL computer program.<sup>16</sup> The three contour diagrams represent the vertical ionization potentials for the  $\text{Br}_2(X^3\Pi_u)$ ,  $\text{Br}_2(A^3\Pi_u)$  and  $\text{Br}_2(B^3\Pi_u)$  electronic states as a function of  $Z$ , the distance between the  $\text{Br}_2$  molecule and the Pt(111) surface, and  $R$ , the internuclear distance between the bromine atoms. The shaded regions on the contour diagrams represent the values of  $Z$  and  $R$  that are resonant with the occupied states of Pt(111), thus favorable for electron transfer from the surface to the incident ion. The vertical dashed lines bracket the highest probability density for the vibrational eigenstates of  $\text{Br}_2^+(X^2\Pi_{g3/2})$ . The projections of these eigenstates onto the neutral potential energy contours completely fall within the shaded region of the  $\text{Br}_2(X^3\Pi_u)$  contour diagram, suggesting highly efficient neutralization to the ground state for both incident vibrational states. Therefore, the formation of  $\text{Br}_2^-$  is not expected to depend on the initial vibrational state, in agreement with the data in Fig. 4.13.

In contrast, the projections of the  $\nu=2$  eigenstates onto the weakly bound  $\text{Br}_2(A^3\Pi_u)$  and  $\text{Br}_2(B^3\Pi_u)$  states suggest that only a small fraction of the incident projectiles prepared in the  $\nu=2$  state will neutralize to either excited state. When  $\text{Br}_2^+(^2\Pi_{g3/2}, \nu=2)$  molecules are compressed to 2.1 Å, they have a very slight chance to neutralize to the  $A$  state, and even a lower probability to neutralize to the  $B$  state. Neutralization to both states is more efficient when the molecule is stretched to 2.3 Å. Since DN is the dominant dissociation mechanism for  $\text{Br}_2^+$  translational energies below 44 eV, then Fig. 4.15 suggests that incident projectiles prepared in the  $\nu=2$  vibrational state will

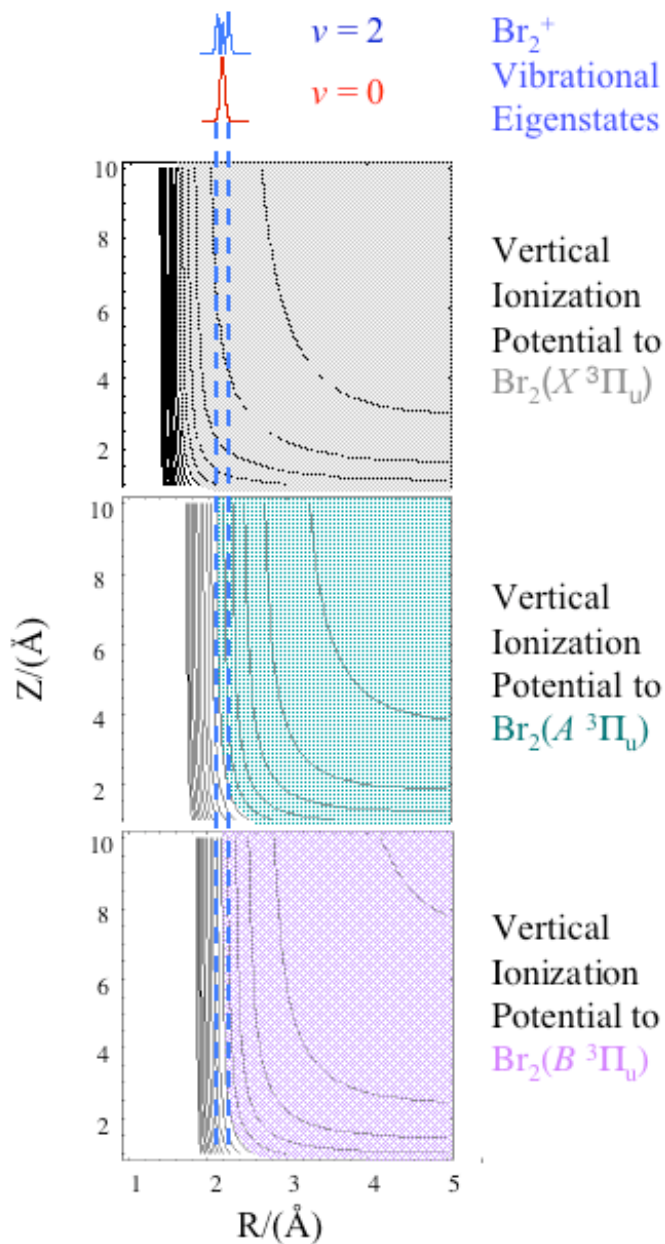


Figure 4.15. The projection of the  $\text{Br}_2^+(^2\Pi_{g/2}, v)$  vibrational eigenstates onto the contour plots for three representative neutral bromine electronic states,  $\text{Br}_2(X^1\Pi_g^+)$ ,  $\text{Br}_2(A^3\Pi_u)$ , and  $\text{Br}_2(B^3\Pi_u)$ . The contour plots represent the vertical ionization potentials (I.P.) from the  $\text{Br}_2^+(^2\Pi_{g/2})$  potential energy curve to the indicated electronic state as a function of the Br<sub>2</sub>-Pt distance,  $Z$ , and the Br-Br internuclear distance,  $R$ . The shaded regions represent the vertical I.P. values that are resonant with the occupied states of the Pt(111) surface.

result in less dissociation of the parent molecule compared to incident projectiles prepared with zero vibrational quanta. This behavior is consistent with the yield ratio for  $\text{Br}^-(^1S_0)$  shown in Fig. 4.13.

The question remains as to why the yield ratio for  $\text{Br}^-(^1S_0)$  in Fig. 4.13 decreases as the incident translational energy decreases. This behavior is explained by the combination of the neutralization process of the incident molecular ion and the second electron capture from the surface to the neutralized molecule. The bromine molecule will most likely dissociate if an electron from the surface occupies a neutral excited state rather than the ground state. As the incident  $\text{Br}_2^+$  translational energy decreases, the bond length of the parent molecule stretches to larger distances before colliding with the surface.

Figure 4.16 illustrates classical trajectory calculations beginning when the bromine molecule is neutralized 5 Å above the surface and ending when the molecule impacts the surface. The solid and dashed curves represent trajectories for  $\text{Br}^+$  incident at 46 eV and 20 eV, respectively. The trajectories commence at Br–Br internuclear distances corresponding to the highest probability densities for the  $v=0$  and  $v=2$  states. The contour diagram represents the vertical electron affinity from the neutral  $\text{Br}_2(A^3\Pi_u)$  state to the  $\text{Br}_2^-(^2\Pi_u^+)$  electronic state as a function of  $Z$  and  $R$ . At the higher collision energy, both the  $\Pi=0$  and  $\Pi=2$  trajectories penetrate deep into the shaded region, indicating efficient electron capture for the fragments. However, when the collision energy decreases, the  $R$  values for the three trajectories at the point of impact are quite different. A comparison of the green and the blue dashed curves indicates that the second electron capture for  $\text{Br}_2^+(^2\Pi_{g3/2}, v=2)$  is more efficient for the decompressed molecule (2.294 Å). However, the probability for electron loss is also more likely for the decompressed  $\Pi=2$  molecule than for  $\Pi=0$ . These combined effects of neutralization, electron capture, and survival probability of the negative ion inhibit  $\text{Br}^-$  formation as the collision energy decreases.

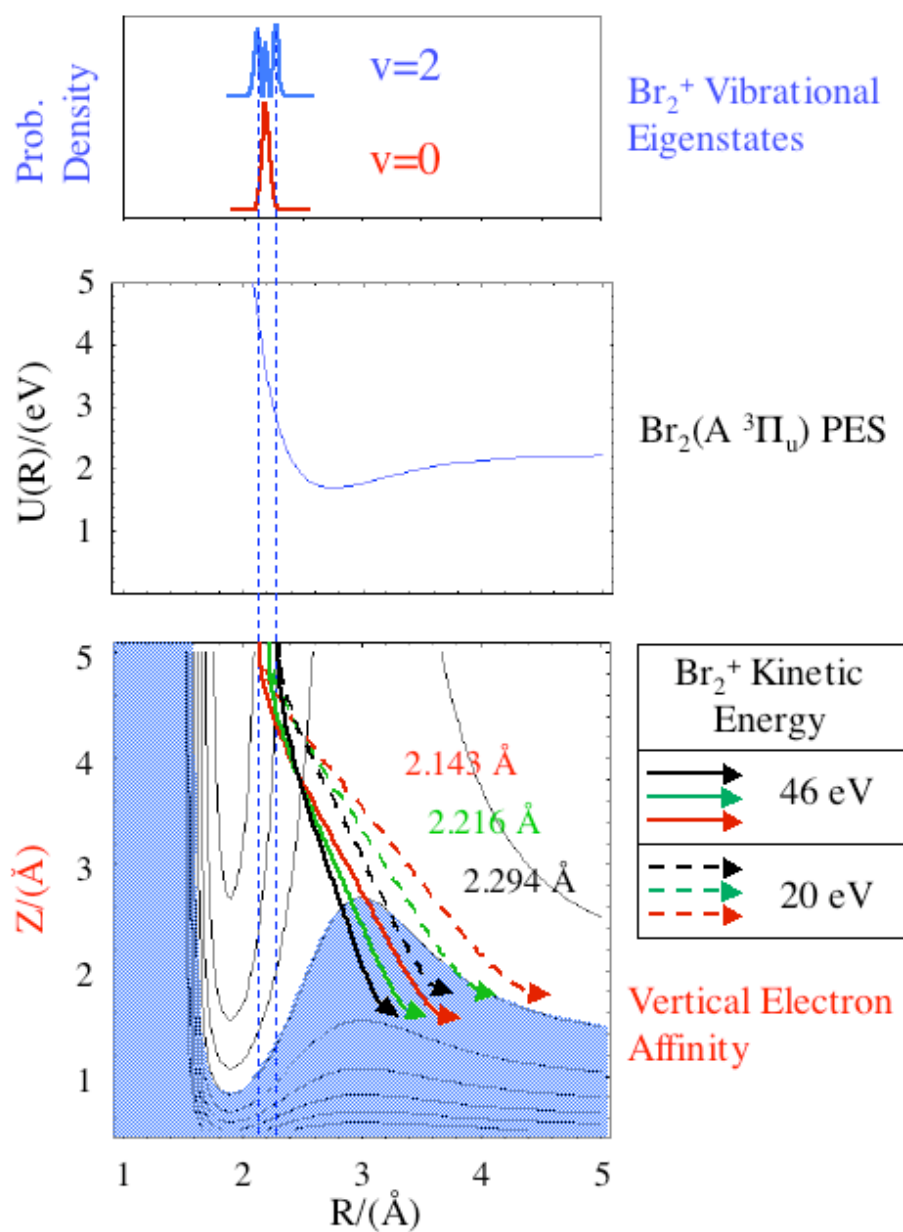


Figure 4.16. The projection of the  $\text{Br}_2^+(^2\Pi_{g/2}, v)$  vibrational eigenstates onto the  $\text{Br}_2(\text{A } ^3\Pi_u)$  state potential energy curve and the vertical electron affinity contour plot. The contour plot represents the vertical electron affinity (I.P.) for the  $\text{Br}_2(\text{A } ^3\Pi_u)$  state to the  $\text{Br}_2^-(^2\Pi_u^+)$  state as a function of the  $\text{Br}_2$ -Pt distance,  $Z$ , and the Br-Br internuclear distance,  $R$ . The shaded region represents vertical E.A. values that are resonant with the occupied states of the Pt(111) surface.

#### 4.4. Comparison of Atomic Versus Diatomic Projectiles

The most intriguing feature observed when state-selected  $\text{Br}_2^+(\text{}^2\Sigma_{g3/2}, \nu)$  and  $\text{Br}^+(\text{}^3P_2)$  scatter from a Pt(111) surface is the very sharp resonance in the emergence of negative ions. This, combined with the enhanced kinetic energies of the products, the focusing behavior of the polar intensity plots, and the extremely high negative ion yield at the peak of the resonance supports a trajectory-dependent charge-transfer mechanism. In order to determine the experimental conditions that lead to this unprecedented scattering behavior, the data are compared for scattering atomic and molecular cations on the Pt(111) surface.

Figure 4.4 compares the bromine anion product yields for the two incident projectiles as a function of the incident projectile velocity. Interestingly, the peak position of the resonance for the  $\text{Br}^-(\text{}^1S_0)$  products resulting from scattering  $\text{Br}^+(\text{}^3P_2)$  is shifted by only 0.5 km/s to higher collision velocities. This minor velocity shift suggests that the resonance feature may arise from a critical collision velocity near 8.0 km/s. When the incident projectile collides with the surface at the critical velocity, the transient deformation of the surface at the point of impact and the motion of the projectiles create an ideal electronic coupling for the efficient formation and survival of negative ions.

A comparison of the exit velocities of the products also confirms the critical timing between the motion of the Pt atoms and the bromine projectiles. Figure 4.5 reveals that for incident collision velocities between 7.5 and 8.0 km/s, the scattered products resulting from both atomic and molecular collisions emerge from the surface with velocities near 2.25 km/s. Regardless of the incident projectile, collisions normal to the surface create similar transient deformations of the surface. Since the scattered products leave the surface with similar velocities, then the critical timing for



efficient electron transfer is not significantly modified for collisions of  $\text{Br}_2^+$  and  $\text{Br}^+$  with the same incident velocity.

Coincident with the resonance feature observed in the product yield data, the products emerge from the surface with the narrowest angular distributions for collisions of both  $\text{Br}_2^+$  and  $\text{Br}^+$  as shown in Fig. 4.7, where the smallest FWHM values correspond to the narrowest angular distributions. This focusing effect of the scattered products arises from the efficient negative ion formation when the incident projectiles collide with a three-fold hollow site on the Pt(111) surface, as confirmed with the three-component curve fits described in Chapter 3. Consistent with the negative ions yield and exit velocity data, the minimum FWHM values for the two projectiles are shifted to higher incident velocities for the atomic projectiles. The most plausible explanation for this shift involves the number of surface atoms disturbed by the collision with the surface. Since the atomic diameter of bromine is 2.28 Å, and the spacing between two Pt atoms on the (111) face is 2.78 Å (see Fig. 3.18), Br can easily collide in the center of a three-fold hollow site disturbing only the three atoms surrounding the point of impact. The collisions involving bromine molecules are likely to displace more than just the atoms at the three-fold hollow site, depending on the molecular orientation. If the axis of the diatomic molecule lies parallel to the surface, then the atoms surrounding two neighboring three-fold hollow sites can be simultaneously disturbed. In addition to the orientation of the molecule, the number of surface atoms involved in the collision also depends on the degree to which the Br atoms separate following DN. For incident energies near 20 eV, the distance between the two bromine atoms at the point of impact is ~4.5 Å, whereas an 80 eV  $\text{Br}_2$  molecule only has enough time to separate a little more than 3 Å before impact with the surface as shown in Figure 4.9. Clearly, the number of surface atoms involved in the bromine collisions will vary for atomic and molecular projectiles.

Since the emergence of negative ions depends on the motion of the surface atoms, then the effects of an increase in the surface temperature should be similar for the two projectiles. Figure 4.17 illustrates the similarity between the yield ratio values for scattering  $\text{Br}_2^+(^2\Pi_{g3/2}, v = 0)$  and  $\text{Br}^+(^3P_2)$  on a 25° C and 400° C Pt(111) surface. Remarkably, the yield ratio values are the same within the error bars for incident velocities between 5.0 and 10.0 km/s. This behavior confirms the sensitivity of the negative ion yield on the motion of the surface atoms. The most pronounced changes in the surface with an increase in the surface temperature is the 0.097 eV change in the vibrational energy for each Pt atom and the thermal disordering of the lattice. The change in the energy of the surface atoms modifies the timing between the movements of the surface atoms and the departing projectiles in a manner that causes the “ideal” electronic coupling to shift to slightly lower collision velocities.

The most unusual observation when comparing the dynamics for the two systems is the increased efficiency for forming  $\text{Br}_2^-$  relative to  $\text{Br}^-$ . At the peak of the resonance feature, 30% of the incident  $\text{Br}_2^+$  ions convert to  $\text{Br}_2^-$  compared to 7% of the incident  $\text{Br}^+(^3P_2)$  ions converted to  $\text{Br}^-(^1S_0)$ . This is contrary to predictions of conventional charge transfer theory for the formation of negative ions based on the electron affinity values for the particles. The formation of  $\text{Br}^-(^1S_0)$  is expected to be more efficient than  $\text{Br}_2^-$ , since the corresponding electron affinities are 3.36 eV and 2.55 eV,<sup>17</sup> respectively. Moreover, the bond dissociation energy for  $\text{Br}_2(X\ ^1\Pi_g^+)$  is relatively low (1.97 eV),<sup>3</sup> suggesting that the collision with the surface should promote the dissociation of the parent molecule, thus reducing the yield of bromine molecular anions. However, this is contrary to the experimental results.

One possible explanation for this difference involves the efficiency of the detector in counting atomic versus molecular bromine particles. When an ion collides with the channel electron multiplier array (CEMA) plates, the impact creates a cascade of  $10^7$  electrons that emerge from the opposite side of the detector before impacting the

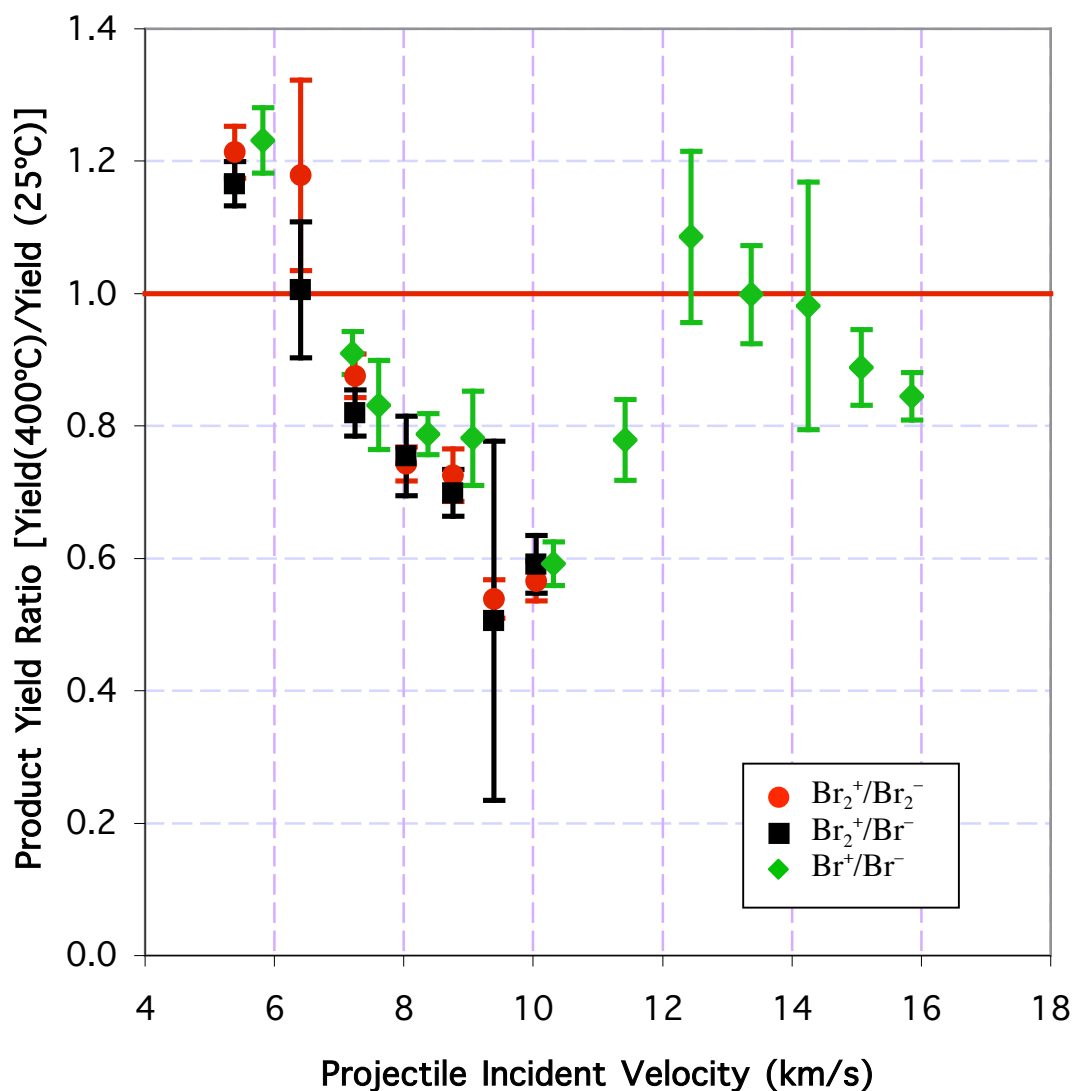


Figure 4.17. The ratio of the product yield at  $T_s=400^\circ\text{C}$  to  $T_s=25^\circ\text{C}$  versus the projectile incident velocity. The circles and squares represent the  $\text{Br}_2^+$  and  $\text{Br}^-(^1S_0)$  yield ratios for scattering  $\text{Br}_2^+(^2\Pi_{g3/2}, v=0)$  on Pt(111). The diamonds represent the  $\text{Br}^-(^1S_0)$  yield ratios for scattering  $\text{Br}^+(^3P_2)$  on Pt(111). The line at 1.0 represents the absence of a temperature effect on the emergence of negative ions.

phosphor screen. If the number of electrons exiting the CEMA plates depends on the mass of the ions, then the number of localized spots on the phosphor screen will not change. However, a change in the number of electrons impacting the phosphor screen may modify the intensity of the images, which would affect the normalization values of the incident ion packets. According to conversations with the manufacturer of the CEMA plates utilized in the experiments, the mass difference between Br and Br<sub>2</sub> will not significantly modify the number of electrons exiting the CEMA plates. This is also consistent with the experimental results described by Fraser for collisions of H<sup>+</sup>, H<sub>2</sub><sup>+</sup>, and H<sub>3</sub><sup>+</sup> on a glass microchannel plate, where the ion induced electron yields do not vary significantly for the three incident projectiles.<sup>18</sup> Moreover, when the yield values are calibrated in the current experiments, the overall intensity of the Br<sub>2</sub><sup>+</sup> and Br<sup>+</sup> incident ion packets are reduced to allow for single ion detection. The number of incident ions is directly correlated to the normalization values obtained for the incident ion packets. Therefore, the calibrated product yield values should not be significantly affected by any minor differences in the efficiency of the detector.

The only explanation that can account for the greater emergence of Br<sub>2</sub><sup>-</sup> is the differences in the electronic coupling between the projectiles and Pt(111). Although the two projectiles are expected to invoke different surface responses to the collision, the absence of density functional theory calculations on a transient surface limits the ability to determine the exact mechanisms that lead to significant differences. In addition to understanding modifications to the Pt(111) density of states, classical trajectory calculations for the Br<sub>2</sub><sup>+</sup>/Pt(111) system will also provide useful details about the modifications to the surface as a result of the heavy atom collision.

## 4.5. Summary

Scattering  $\text{Br}_2^+(^2\Pi_{g3/2}, v = 0 \text{ and } 2)$  on Pt(111) reveals another system with an extraordinary resonance in the product yields. Coincident with the resonance, the  $\text{Br}_2^-$  and  $\text{Br}^-(^1S_0)$  products leave the surface with enhanced exit velocities and the narrowest angular distributions. The  $\text{Br}_2^-$  exhibits all the signatures of the trajectory-dependent scattering mechanism described in Chapter 3. Therefore, the resonance feature for  $\text{Br}_2^-$  is assigned to trajectories that collide with a three-fold hollow site, thus causing the products to scatter from the surface with the narrowest angular distributions. The transient deformation of the surface and the motion of the departing molecule modify the electronic coupling in a manner that either creates efficient electron transfer or inhibits electron loss at the peak of the resonance. Two dissociation mechanisms are implicated for the emergence of  $\text{Br}^-$ —DN below 7.2 km/s and CID above this collision velocity. The inhibition in the  $\text{Br}^-$  product yield when the incident vibrational energy increases also supports a DN mechanism for collision energies below 30 eV.

The parallels between the data for scattering  $\text{Br}_2^+$  and  $\text{Br}^+$  reveal the most critical parameters for observing the anomalous resonance. The peaks of the resonance feature occur for collision velocities near 8.0 km/s and product exit velocities near 2.25 km/s. Our experimental geometry that employs normal incidence and normal detection is ideal for probing local electron transfer effects at the point of impact on the surface. The dependence of the product yield on surface temperature indicates that increased vibrational motion of the surface modifies the charge transfer dynamics. In order to gain additional insight into this intriguing scattering behavior, experiments are warranted that modify the work function of the surface, the crystalline orientation of the surface, and the mass ratios of the projectile to the surface atoms.

## 4.6. References

- <sup>1</sup> A. W. Potts and W. C. Price, Transactions of Faraday Society **46**, 1242 (1971).
- <sup>2</sup> M. V. Kurepa, D. S. Babic, and D. S. Belic, Journal of Physics B-Atomic Molecular and Optical Physics **14** (2), 375 (1981).
- <sup>3</sup> E. S. Chen and E. C. M. Chen, Journal of Physical Chemistry A **107** (1), 169 (2003).
- <sup>4</sup> J. E. Smedley, H. K. Haugen, and S. R. Leone, Journal of Chemical Physics **87** (5), 2700 (1987).
- <sup>5</sup> R. J. L. Roy, R. G. Macdonald, and G. Burns, Journal of Chemical Physics **65** (4), 1485 (1976).
- <sup>6</sup> B. G. Koenders, G. J. Kuik, K. E. Drabe, and C. A. Delange, Chemical Physics Letters **147** (4), 310 (1988).
- <sup>7</sup> M. Maazouz, P. L. Maazouz, and D. C. Jacobs, The Journal of Chemical Physics **117** (24), 10917 (2002).
- <sup>8</sup> J. S. Martin, J. N. Greeley, J. R. Morris, B. T. Feranchak, and D. C. Jacobs, Journal of Chemical Physics **100** (9), 6791 (1994).
- <sup>9</sup> J. R. Morris, G. Kim, T. L. O. Barstis, R. Mitra, C. L. Quinteros, and D. C. Jacobs, Nuclear Instruments & Methods in Physics Research Section B- Beam Interactions with Materials and Atoms **125** (1-4), 185 (1997); H. Akazawa and Y. Murata, Journal of Chemical Physics **92** (9), 5560 (1990); P. H. F. Reijnen, U. Vanslooten, and A. W. Kley, Journal of Chemical Physics **94** (1), 695 (1991); V. Grill, J. Shen, C. Evans, and R. G. Cooks, Review of Scientific Instruments **72** (8), 3149 (2001).
- <sup>10</sup> A. Kokalj and M. Causa, Journal of Physics: Condensed Matter **11**, 7463 (1999).
- <sup>11</sup> E. Hwang, P. J. Dagdigan, and J. Tellinghuisen, Journal of Molecular Spectroscopy **181** (2), 297 (1997).
- <sup>12</sup> J. R. Morris, G. Kim, T. L. O. Barstis, R. Mitra, and D. C. Jacobs, Journal of Chemical Physics **107** (16), 6448 (1997).
- <sup>13</sup> J. F. Ziegler, J. P. Biersack, and U. Littmark, *The Stopping and Range of Ions in Solids*. (Pergamon Press, New York, 1985).

- <sup>14</sup> I. WaveMetrics, IGOR Pro (Lake Oswego, OR, 1988-2000).
- <sup>15</sup> J. N. Greeley, J. S. Martin, J. R. Morris, and D. C. Jacobs, *Surface Science* **314** (1), 97 (1994).
- <sup>16</sup> R. J. LeRoy, LEVEL (University of Waterloo, Canada, 2001).
- <sup>17</sup> *CRC Handbook of Chemistry and Physics*, edited by D. R. Lide (CRC Press, New York, 1999).
- <sup>18</sup> G. W. Fraser, *International Journal of Mass Spectrometry* **215** (1-3), 13 (2002).